Journal of Advanced Ceramics
2020, **9**(2): 129–148
https://doi.org/10.1007/s40145-020-0365-x

ISSN 2226-4108
CN 10-1154/TQ

Review

Ruddlesden–Popper phase A_2BO_4 oxides: Recent studies on structure, electrical, dielectric, and optical properties

Gurudeo NIRALA, Dharmendra YADAV, Shail UPADHYAY*

Department of Physics, *Indian Institute of Technology (BHU)*, *Varanasi-221005*, *India*

Received: October 1, 2019; Revised: January 29, 2020; Accepted: February 4, 2020
© The Author(s) 2020.

Abstract: In the last two decades, structure and properties of Ruddlesden–Popper phase (RP) A_2BO_4 oxides with K_2NiF_4 structure, have been widely investigated. But to the best of our knowledge, no review article is available in the literature on recent studies on these oxides. Therefore, in this article, recent studies on structure, electrical, dielectric, and optical properties of these oxides have been reviewed. Special attention is put on to highlight the effect of doping and oxygen stoichiometry on the structure and properties of these oxides. Further, important applications of these oxides have also been mentioned in this article.

Keywords: Ruddlesden–Popper (RP) phase; A_2BO_4 oxides; electrical conductivity; dielectric

1 Introduction

Ruddlesden–Popper (RP) phases are described with the general formula of $A_{n+1}B_nO_{3n+1}$. This formula can also be written as $AO(ABO_3)_n$, where n perovskite layers are stacked between AO rock-salt layers along the crystallographic c-axis [1]. The first member of the series, A_2BO_4 ($n = 1$), adopts the K_2NiF_4 structure. Figure 1 represents the ideal tetragonal unit-cell of a RP-phase A_2BO_4 oxide, which corresponds to the stoichiometric compound crystalized in $I4/mmm$ space group. This is also a two-dimensional (2D) layered perovskite structure. Commonly, A_2BO_4 oxides consist of rare or alkaline earth element as A-site cations with transition or post-transition metals on the B-site, forming an extensive series of compositions. The A-site cations have a coordination number of "9", locating at the boundary between the two types of layers, while the B-site cations are positioned at the center of an octahedron formed by six oxygen anions. RP oxides have shown very attractive and versatile physical properties such as superconductivity [2–6], magnetoresistance [7–11], mixed ionic and electronic conductivity [12–15], giant and colossal dielectric [16–19], low loss microwave dielectric [20–24], photoluminescence [25–29], catalytic activity [30–32], thermoelectric [33–35], etc., which are useful for many energy and electronic devices. The A_2BO_4 layered perovskites have recently attracted attention owing to their great environmental stability and versatile applications. The alkaline earth element (AE) doped and undoped RE_2MO_4 layered perovskites (where RE is rare earth element and M is transition metal) have been considered as alternatives for cathode application in Solid Oxide Fell Cells (SOFC)/Solid Oxide Electrolysis Cells (SOEC), due to their superior mixed ionic and electronic conductivities in comparison to traditionally used perovskite oxides [36–39]. Sr_2CeO_4, AE_2SnO_4 ($AE = Ca, Sr, Ba$) are found to be suitable host for photoluminescence applications

* Corresponding author.
E-mail: supadhyay.app@itbhu.ac.in

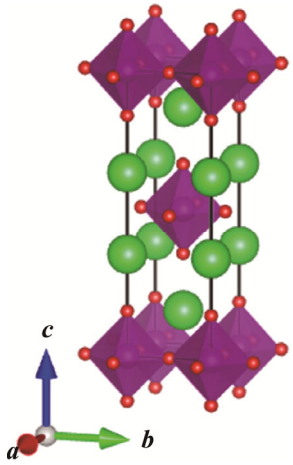

Fig. 1 Ideal tetragonal unit cell of stoichiometric A_2BO_4 layered perovskite crystalized in $I4/mmm$ space group.

[40–42]. Doped and undoped lanthanide nickelates show giant/colossal dielectric properties [43–45].

In the last several years, rapid growth in solar cells and optoelectronic devices based on 3D organic–inorganic halide-based perovskites is observed. But their inherent instabilities over moisture, light, and heat strongly hindered this growth. Recently 2D organic–inorganic based layered perovskites received increasing attention owing to their superior ambient stability. These 2D perovskites have demonstrated to exhibit abundant and tunable optoelectronic properties, high quantum efficiency, and large specific surface area, which hold a good prospect for a range of electronic and optical applications [46,47].

During 1980–1990, Rao and his group [48,49] carried extensive research work on structure and magnetic properties of A_2BO_4 oxides. Magnetic properties of these oxides were investigated more extensively than transport properties. They published a few review articles and chapters in the book on these oxides [50]. After observation of superconductivity up to 35 K in the Ba-doped La_2CuO_4 ternary compound by George Bednorz and Alex Müeller of IBM Zurich Laboratory in 1986 [51], research works on A_2BO_4 oxides further intensified. However, in the last two decades, these oxides have attracted attention because of their applications based on their electrical, optical, and dielectric properties. Recently two review articles have been published in the literature on diffusion/transport of oxide ion [52,53]. To the best of our knowledge, no recent review articles on the overall development of structure, properties, and applications of A_2BO_4 layered perovskites are available in the literature. Therefore, in this article structure, electrical, dielectric, and optical properties of A_2BO_4 along with various applications have been reviewed. In addition, various strategies for enhancing their properties using suitable doping at A- as well as B-sites are discussed. We expect that this article will intensify research on A_2BO_4 layered perovskites and finally commercialization of devices based on these oxides.

2 Structure and oxygen stoichiometry

The A_2BO_4 compounds crystallize in two major structural forms: T-type and T′-type [54]. The schematic structure of T-type La_2NiO_4 ternary oxide is shown in Fig. 2(a). For clarity, only half cell ($a/2 \times b/2 \times c$) is shown. The Ni cations are located at the center of apically elongated octahedra, also known as NiO_6 octahedra; the six $Ni-O$ distances are: $Ni-O_{bs}(O(1)) \times 4 = 1.947$ Å and $Ni-O_{ap}(O(2)) \times 2 = 2.267$ Å; two long distant atoms are along the c-axis. The La cation is surrounded by nine oxygen atoms, four O_{ap} atoms (in the same level of La atom), four O_{bs} atoms (in Ni level, above (below)), and one O_{ap} atom (head-below (head-above) from La atom). These nine O atoms make a LaO_9 polyhedra. The La atom is not located at the center of this polyhedra, but it is little shifted towards the capping O_{ap}. The NiO_6 octahedra and LaO_9 polyhedra share faces with each other and each NiO_6 octahedra is connected with four nearest neighboring NiO_6 octahedra in ab-plane by common shared O_{bs} atoms. Each NiO_6 octahedra with eight La atoms of O_{ap} level makes a $LaNiO_3$ perovskite unit. Between two perovskite units, there is a LaO rocksalt layer in ab-plane. Therefore, the

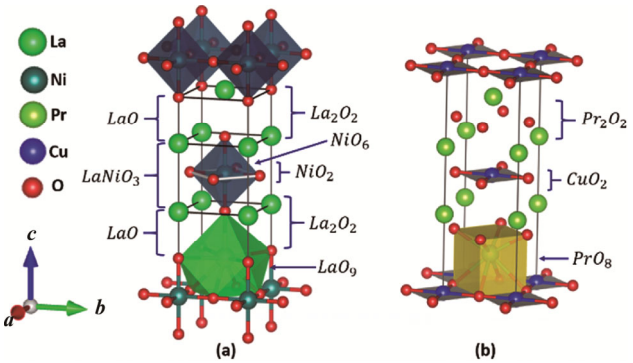

Fig. 2 (a) Half unit cell of T-type La_2NiO_4 layered perovskite. (b) Unit cell of T′-type Pr_2CuO_4 ternary oxide.

La_2NiO_4 structure can be described as an intergrowth of an alternative layer of $LaNiO_3$ perovskite and LaO rocksalt along the c-axis. Thus T-type A_2BO_4 ternary oxides are known as A_2BO_4 layered perovskite or RP-phase layered perovskite. K_2NiF_4 has a similar structure. Hence, this structure is also commonly referred as K_2NiF_4 structure.

In contrast to T-type structure in T′-type structure, the cationic arrangement is the same, but the anionic arrangement is different [55]. Basal oxygens, O_{bs}, do not change its position but apical oxygens, O_{ap}, are shifted to the face of the unit cell, between the levels of cation A, designated as O_f. The schematic structure of T′-type Pr_2CuO_4 ternary oxide is shown in Fig. 2(b). The Cu cation is surrounded by four O_{bs} atoms and their interionic distances are 1.98 Å. The Pr cations are surrounded by eight O atoms: four O_{bs} atoms are in the Cu level and four O_f are between the level of Pr atoms, making a PrO_8 cube.

The A_2BO_4 compounds can also be visualized as alternative stacking of BO_2 and A_2O_2 bilayers along c-axis [56]. In La_2NiO_4, four halves shared (between unit cells) O_{bs} atoms and one Ni atom makes NiO_2 layer, similarly two O_{ap} and two La atoms make La_2O_2 bilayer, as shown in Fig. 2(a), so the structure of La_2NiO_4 compromises the following sequences of layers.

$$(NiO_{bs})_o(LaO_{ap})_c(LaO_{ap})_o(NiO_{bs})_c(LaO_{ap})_o$$
$$(LaO_{ap})_c(NiO_{bs})_o \ldots$$

The subscript o and c indicate whether the cation is at the origin or center of the mesh, respectively. Similar stacking of BO_2 and A_2O_2 bilayers in T′ -type structured Pr_2CuO_4 is also schematically shown in Fig. 2(b). The A_2BO_4 compounds also crystalize in T*-type of structure, which is a hybrid of T- and T′ -type structure [54]. Recently several research groups have investigated the T- and T′-type structures using well known Goldschmidt tolerance factor *t* as a criterion. The tolerance factor is based on the analysis of perovskite supercells (also known as perovskite tolerance factor) and given as follows [57]:

$$t = \frac{r_A + r_O}{\sqrt{2}(r_B + r_O)} \quad (1)$$

where, r_A,r_B, and r_O are ionic radii of cation A, cation B, and oxygen, respectively. The tolerance factor "t" for T- type structure is found in the range of $0.99 \geq t \geq 0.87$ while for T′ -type structure the tolerance factor lies in the range of $0.86 > t \geq 0.83$. Under high pressure, the lower limit of t for T′-type structure extends up to 0.81. The T*-type structure exists for a narrow range of tolerance factors, lies in between the t of T- and T′-type structure [54].

Most of the A_2BO_4 layered perovskites crystallize either in orthorhombic structure or in tetragonal structure. The tolerance factor t for tetragonal and orthorhombic structure lies in the range of $0.99 \geq t \geq 0.88$ and $0.88 \geq t \geq 0.865$, respectively [56]. The A_2BO_4 layered perovskites can be further subdivided in two groups, one of which consists rare earth element (RE = La, Nd, Pr, etc.) as cation "A" and the other of which consists alkali earth element (AE = Ca, Sr, Ba) as cation "A". The layered perovskites consisting RE as cation "A", consist transition metal(s) (M = Ni, Cu, Co, etc.) in divalent state as cation "B" and the other group which consist AE as cation "A", consists of transition element(s) or post-transition element(s) (M′ = Mn, Sn, Ti, etc.) in the tetravalent state, as cation "B". These two groups of layered perovskites are named as RE_2MO_4, and $AE_2M'O_4$ in this article, respectively. In recent years another group of A_2BO_4 layered perovskites or doped A_2BO_4 layered perovskites are also studied, which consist of both rare earth and alkaline earth elements in the form of cation "A" and cation "A'" in equal or unequal stoichiometries. The general structural formula for this group of compounds is sometimes written as "$A_xA'_{2-x}BO_4$". Majority of RE_2MO_4, crystallize in orthorhombic structure with space group $Bmab, P4_2/ncm, Pccn,$ etc. while $AE_2M'O_4$ crystallize in tetragonal structure with space group $I4/mmm, P4/mmm,$ etc. There are also some exceptions as well, marked as "*" in Table 1, which do not follow this general categorization.

In orthorhombic RE_2MO_4, tensile stress in the RE_2O_2 layer and compressive stress in the MO_2 layer are present. In La_2NiO_4, the basal $Ni - O_{bs}$ interatomic distances (1.94 Å) are shorter than the sum of the ionic radii (2.09 Å, using $r_{Ni^{2+}} = 0.73$ Å and $r_{O^{2-}} = 1.40$ Å) and three out of four basal $Li - O_{ap}$ interatomic distances (2.797 Å and 3.15 Å) are longer than the sum of the ionic radii (2.62 Å, using $r_{La^{2+}} = 1.216$ Å) [58,59]. This mismatch of interionic distances and the sum of ionic radii produces stress between interlayers. These interlayer stresses are partially relieved by the systematic canting of NiO_6 octahedra about a fixed rotation axis, which is parallel to the basal plane, i.e., the NiO_2 and La_2O_2 layers are partially buckled to relieve the compressive and

Table 1 Structure, highest experimentally measured electrical conductivity, and activation energy of recently studied ceramics

Ceramic	Structure	Total electrical conductivity, σ ($S \cdot cm^{-1}$) at temperature (℃)	Activation energy, E_a (eV)	Reference
$Nd_2NiO_{4.2}$	Orthorhombic	99 at 900	0.081	[12]
$Nd_{1.7}Ca_{0.3}NiO_{4.11}$	Tetragonal	153 at 900	0.085	[12]
$(Nd_{0.9}La_{0.1})_2Ni_{0.75}Cu_{0.25}O_4$	Tetragonal	114.36 at 500	0.083	[96]
$Nd_2Ni_{0.9}Co_{0.1}O_4$	Orthorhombic	48 at 400	0.145	[97]
$Nd_2Ni_{0.9}Cu_{0.1}O_4$	Orthorhombic	42 at 400	0.111	[97]
$Nd_{1.8}Sr_{0.2}Ni_{0.6}Cu_{0.4}O_{4.01}$	Tetragonal	42.7 at 640	0.07	[76]
$Nd_2Ni_{0.9}Fe_{0.1}O_4$	Orthorhombic	38 at 400	0.109	[97]
$Nd_{1.8}Ce_{0.2}Cu_{0.5}Ni_{0.5}O_{4+\delta}$	Tetragonal	0.619 at 700	0.11	[75]
$Nd_2Ni_{0.9}Mn_{0.1}O_4$	Orthorhombic	38 at 400	0.119	[97]
La_2NiO_4	Orthorhombic	96 at 800	0.07	[98]
$La_2Ni_{0.8}Cu_{0.2}O_4$	Orthorhombic	57 at 800	0.08	[98]
$La_2Ni_{0.5}Cu_{0.5}O_4$	Orthorhombic	55 at 400	0.09	[99]
$La_{1.2}Sr_{0.8}NiO_4$	Tetragonal	180 at 800	0.073	[100]
$La_2Ni_{0.98}Mg_{0.2}O_4$	Orthorhombic	88.2 at 400	0.061	[101]
$Pr_{1.3}Sr_{0.7}NiO_4$	Tetragonal	0.25 at 900	0.065	[102]
$Pr_{1.9}Ni_{0.75}Cu_{0.25}O_4$	Tetragonal	100 at 500	0.64	[15]
$Pr_{1.9}(Ni_{0.75}Cu_{0.25})_{0.95}Ga_{0.05}O_4$	Tetragonal	40 at 500	0.57	[15]
$Pr_2Ni_{0.5}Cu_{0.5}O_4$	Orthorhombic	130 at 450	0.08	[99]
$Pr_{1.3}Sr_{0.7}Ni_{0.7}Cu_{0.3}O_4$	Tetragonal	260 at 700	0.06	[103]
$Sm_{1.5}Sr_{0.5}NiO_4$	Orthorhombic	0.361 at 640	0.26	[104]
$La_{1.5}Sr_{0.5}CoO_4$	Tetragonal	0.03 at 400	0.451	[17]
$Nd_{0.8}Sr_{1.2}CoO_{4+\delta}$	Tetragonal	212 at 800	0.51	[105]
$PrSrCo_{0.5}Mn_{0.5}O_{4.03}$	Tetragonal	7 at 900	0.42	[106]
$Pr_{0.5}Sr_{1.5}Co_{0.5}Mn_{0.5}O_4$	Tetragonal	23 at 900	0.34	[106]
La_2CuO_4	Orthorhombic	10 at 900	0.07	[107]
$La_{1.9}Pr_{0.1}Cu_{0.9}Co_{0.1}O_{4.04}$	Tetragonal	1.8 at 900	0.20	[108]
$Pr_{2-x}Sr_xCu_{1-x}Co_xO_4 (x = 0.5, 0.75)$	Tetragonal	25 at 900	0.44	[108]
$Pr_2CuO_{4.05}$	Tetragonal*	200 at 1000	0.34	[107]
$Nd_2CuO_{4.04}$	Tetragonal*	100 at 1000	0.60	[107]
$Sm_{1.8}Sr_{0.2}CuO_4$	Tetragonal	6.8 at 640	0.40	[13]
$Sm_{1.9}Ce_{0.1}CuO_4$	Tetragonal	96 at 950	0.32	[109]
$La_{0.6}Sr_{1.4}MnO_4$	Tetragonal	5 at 1100	0.11	[110]
$Nd_{0.5}Sr_{1.5}MnO_4$	Tetragonal	33.4 at 800	0.20	[111]
$NdBaInO_4$	Monoclinic	3.6×10^{-5} at 858	0.91	[112]
$Nd_{0.9}Ca_{0.1}BaInO_{3.95}$	Monoclinic	4.9×10^{-4} at 500	0.77	[113]
$Nd_{0.9}Ba_{0.1}InO_{3.95}$	Monoclinic	1.3×10^{-4} at 500	0.92	[113]
$Nd_{0.9}Sr_{0.1}BaInO_{3.95}$	Monoclinic	3.0×10^{-4} at 500	0.73	[113]

tensile stresses, respectively, as shown in Fig. 3 [60,61].

The other RE_2MO_4, with similar interlayer stresses as in La_2NiO_4, the systematic canting of MO_6 octahedra are also there, to relieve interlayer stresses in their structure [56]. These distortions in the structure produced by the systematic canting of MO_6 octahedra lead to the change in $Bmab, P4_2/ncm, Pccn$, and $Fmmm$ symmetries of the orthorhombic structure. The two nearest neighbor corner shared MO_6 octahedra generally cant symmetrically in opposite directions

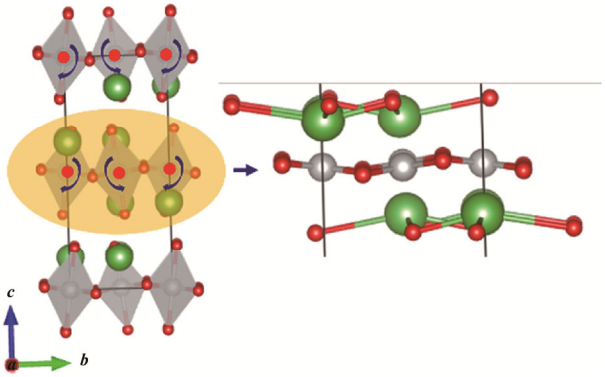

Fig. 3 Schematic diagram of systematic canting of MO_6 octahedra. The buckling of MO_2 and RE_2O_2 interlayers is highlighted in magnified part of image.

about the fixed rotation axis, as shown in Fig. 3. The azimuthal orientation of rotation axes for neighboring planes of MO_6 octahedra differ by 0° in $Bmab$, 90° in $P4_2/ncm$, and between 0° to 90° in $Pccn$. These octahedra canting symmetries are also characterized by long-range ordering. When either distortion is present or correlation length of canting is short, then the structure is best described by the $Fmmm$ symmetry. The $Fmmm$ symmetry is also used in assigning an average structure of the material, with uncharacterized incommensurate structure or presence of weak supercell having a dimension larger than $\sqrt{2}a \times \sqrt{2}b \times c$ [61].

Majority of A_2BO_4 layered perovskites which crystallized in orthorhombic structure transform into the less ordered orthorhombic structure of $Fmmm$ space group above the room temperature and into a tetragonal structure at moderately high temperature. These structural transformations are referred by abbreviated name as LTO (Low-Temperature Orthorhombic), LTLO (Low-Temperature Less Orthorhombic), and HTT (High-Temperature Tetragonal) for general nomenclature [61]. At high temperature (above room temperature) above-mentioned stresses between the interlayers relaxed due to the thermal expansion of the unit cell and the MO_6 octahedra aligned in tetragonal symmetry groups ($I4/mmm$ *or* $P4/mmm$). The alignment of MO_6 octahedra disturb the periodic symmetry and produces structural transformations, initially in LTLO above the room temperature and finally in HTT at high moderately temperature. Stoichiometry of oxygen in the structure is also responsible for the structural transformation. But temperature-dependent structural transitions mentioned above are independent of oxygen stoichiometry due to the thermal expansion of unit cell [58,60–63].

The A_2BO_4 layered perovskites are generally synthesized via solid-state reaction method. During high-temperature synthesis processes ($>$ 1000 ℃), excess oxygens may accommodate in the structure at the interstitial sites and/or oxygen vacancies are created in the structure. These excess oxygens in the structure are accommodated in the form of doubly ionized oxide ions, O_i^{2-}. In this article, Kröger–Vink notation has been followed to represent charge species and defects. In Kröger–Vink notation, the positively charged species are marked as "•" in superscript. Similarly, the negatively charged species are marked as " ′ " in superscript. When an oxide ion, O_i'' accommodates the interstitial sites, two excess holes, $h^\bullet$ are created in the structure. Similarly, when an oxygen vacancy, $V_o^{\bullet\bullet}$ is created two excess electrons, e' are created in the structure. Generation of these defects are represented by Eqs. (2) and (3) [64].

$$\frac{1}{2}O_2(g) = O_i'' + 2h^\bullet \quad (2)$$

$$O_o^\times = V_o^{\bullet\bullet} + \frac{1}{2}O_2(g) + 2e' \quad (3)$$

These excess holes may recombine with electrons or with divalent transition metal ions according to Eqs. (4) and (5), respectively;

$$h^\bullet + e' = 0 \quad (4)$$

$$M^{2+} + h^\bullet = M^{3+} \quad (5)$$

In RE_2MO_4, RE_2O_2 bilayer is electropositive and MO_2 layer is electronegative. Excess oxide ions mostly accommodate in the RE_2O_2 bilayer interstitials and holes generally go in the MO_2 layer due to their electropositive and electronegative nature, respectively. By this mechanism, excess oxide ions in the structure facilitate in neutralizing the electronic polarity of layers. It is also repoted that in RE_2MO_4 oxides, excess oxide ions at interstitial sites minimize the electronic polarity between the RE_2O_2 and MO_2 intergrown layers [65,66]. There are also reports on RE_2MO_4, in which the creation of oxygen vacancies at basal oxygen sites, i.e., in MO_2 layers is discussed [67]. The electronic polarity of intergrown RE_2O_2 and MO_2 layers, inhibits the creation of oxygen vacancy in RE_2O_2 bilayer [66]. Location of oxygen vacancy and interstitial oxygen is schematically shown in Fig. 4 [66]. The oxygen stoichiometry of RE_2MO_4 depends on the number of excess oxide ions at interstitial sites and number of oxygen vacancies in the structure. The interstitial oxide ions O_i'', in RE_2O_2 bilayers play crucial role in reducing the stresses produced by the above-mentioned mismatch

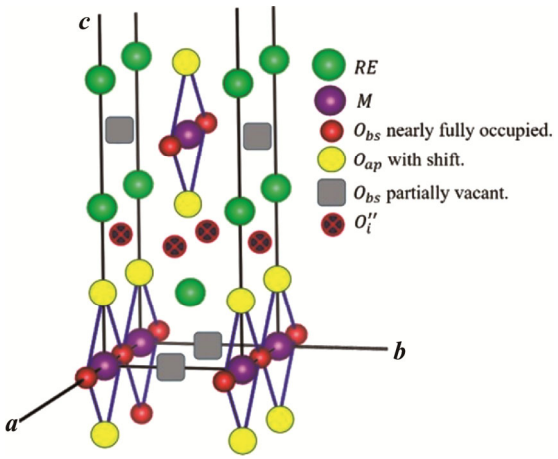

Fig. 4 Schematic representation of location of oxygen vacancies and interstitial oxide ions in A_2BO_4 layered perovskite. Reproduced with permission from Ref. [66], © Royal Society of Chemistry 1994.

of interionic distances of $RE-O_{ap}$ and $M-O_{bs}$ [66]. On the accommodation of oxygen at interstitial sites, the electrostatic repulsion between O_i'' and neighboring apical oxygen O_{ap} of RE_2O_2 bilayer increases the lattice parameters "a" and "c" which facilitates to release of compressive and tensile stresses present in MO_2 layer and RE_2O_2 bilayer, respectively. It is also known that ionic radii of transition metal ions in lower oxidation state are smaller than their higher oxidation state. Hence, oxidation of transition metal ions reduces the effective interionic distances of $M-O_{bs}$. Due to these two processes taking place simultaneously majority of RE_2MO_4 oxides exhibit a structural transformation with increasing concentration of interstitial oxide ions [60,68,69]. For example, the hyper-stoichiometric (oxygen excess) $La_2NiO_{4+\delta}$ ($0.10<\delta<0.15$) transforms from orthorhombic to tetragonal phase [70]. The A_2BO_4 layered perovskites also exhibit a structural transformation on becoming hypo-stoichiometric (oxygen deficient). For example, when Sr_2MnO_4 becomes hypo-stoichiometric, i.e., $Sr_2MnO_{3.5}$, transforms from tetragonal to monoclinic phase [71,72].

The oxygen stoichiometry in structure can also be tailored by substitutions at A and B sites. There are three kinds of substitutions (isovalent, donor, and acceptor) having been done in A_2BO_4 layered perovskites. Further, in the case of isovalent substitution, substituted ion may have smaller or larger ionic radius than the host ion. Isovalent substitution of smaller ionic radii helps in increasing the void space of interstitial sites, thus, supporting accommodation of higher concentration of excess oxygen in the structure. The substitution of larger ionic radii has vice versa effect. The isovalent substitution also helps in increasing or reducing the above-mentioned stresses of intergrown layers, due to increment or decrement in interionic distances, respectively. For example, on substitution of Ni in $La_2Cu_{1-x}Ni_xO_{4+\delta}$ oxygen content increases with the increasing content of Ni. The size of octahedra with Ni gets reduced due to the smaller ionic radius of Ni ($r_{Ni^{2+}}=0.69$ Å) as compared to Cu ($r_{Cu^{2+}}=0.73$ Å). Thus, void space in La_2O_2 bilayer is increased and facilitates easier accommodation of O_i'' [68].

The donor substitutions are generally done in $AE_2M'O_4$ by substituting RE ions at the AE site. The RE substitution creates excess electrons in the structure according to Eq. (6). These excess electrons may reduce M'^{4+}cation to M'^{3+}, according to Eq. (7). On account of this, the $RE_xAE_{2-x}O_2$ rocksalt bilayer becomes electropositive and $M'^{3+}_yM'^{4+}_{1-y}O_2$ becomes electronegative, which helps in accommodating more O_i'' in $RE_xAE_{2-x}O_2$ rocksalt bilayers. For example, $La_xSr_{2-x}MnO_{4+\delta}$, ($0.25\le x\le 0.6$) consist of excess oxygen in the structure as compared to Sr_2MnO_4 [39]. Excess electrons created due to RE substitution do not only reduces M' cations, but also some of them may recombine with excess holes (according to Eq. (4)) created by interstitial oxide ions (according to Eq. (2)). If these two processes of reduction of M'^{4+} cation and recombination of electron and hole occurring simultaneously (may make $x\neq y$), the concentration of reduced M' ion can be different from twice of concentration of RE substituent.

$$RE_2O_3 = 2(RE^{3+}_{AE^{2+}})^{\bullet} + 2O^{*}_{o} + \frac{1}{2}O_2(g) + 2e' \quad (6)$$

$$(M'^{4+}_{M'^{4+}})^{\times} + e' = (M'^{3+}_{M'^{4+}})' \quad (7)$$

The acceptor substitutions in RE_2MO_4 have been made by replacing RE ions with AE ions. Acceptor dopants normally create excess holes in the structure according to Eq. (8). These excess holes recombine with neutral oxygen vacancies and help them stabilizing as $V_o^{\bullet\bullet}$, according to Eq. (9). Another possibility is that these excess holes recombine with divalent (M^{2+}) ions to form trivalent ions (M^{3+}) as given by Eq. (10). The study of $Nd_{2-x}Sr_xNiO_{4-\delta}$ ceramics confirms this hypothesis. This solid solution is an oxygen-deficient material and the content of oxygen decreases with increasing Sr content [73]. $La_{2-x}Sr_xCuO_{4-\delta}$ was studied by Kanai *et al.* [74] as a function of Sr content, oxygen partial pressure, and temperature. This study shows that it is an oxygen deficient material for

$x > 0.5$ in $-6 < \log(P(O_2)/\text{atm}) < 0$ partial pressure range at 900 ℃. The variation of oxygen content with oxygen partial pressure is shown in Fig. 5. Similar to $Nd_{2-x}Sr_xNiO_{4-\delta}$, $La_{2-x}Sr_xCuO_{4-\delta}$ also becomes more oxygen deficient with increasing Sr content.

$$AEO = \left(AE^{2+}_{RE^{3+}}\right)' + \frac{1}{2}O_2(g) + h^{\bullet} \quad (8)$$

$$V_O^{\times} + 2h^{\bullet} = V_O^{\bullet\bullet} \quad (9)$$

$$(M^{2+}_{M^{2+}})^{\times} + h^{\bullet} = (M^{3+}_{M^{2+}})^{\bullet} \quad (10)$$

3 Electrical properties

In the beginning of twenty-first century $A_2BO_{4\pm\delta}$ layered perovskites renewed their interest after the investigation of oxygen transport properties of $La_2NiO_{4\pm\delta}$ at high temperature [75–77]. Electrical properties of $A_2BO_{4\pm\delta}$ layered perovskites at low temperature were extensively studied after the discovery of superconductivity in $La_2CuO_{4\pm\delta}$. But in recent years, more attention has been focused on the study of high-temperature electronic and oxide ion transport properties of $A_2BO_{4\pm\delta}$ layered perovskites. In this context, $La_2NiO_{4\pm\delta}$ is widely studied for their phase stability, oxygen stoichiometry and high-temperature transport properties, and a comparative study with $La_2CuO_{4\pm\delta}$ is established. $La_2NiO_{4\pm\delta}$ shows a semiconductor to metal-like transition at 350 ℃ and have electrical conductivity 100 $\Omega^{-1}\cdot cm^{-1}$ at transition temperature which is lower than

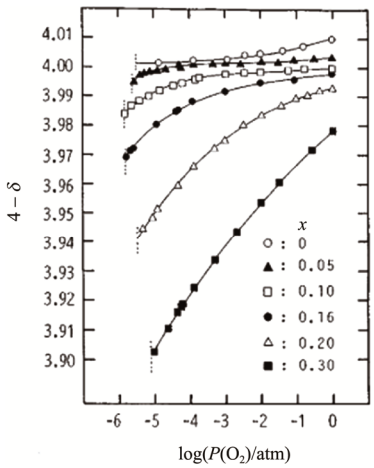

Fig. 5 Oxygen content in $La_{2-x}Sr_xCuO_{4-\delta}$ as a function of oxygen partial pressure at 900 ℃. Oxygen deficiency is increasing with increasing Sr content. Reproduced with permission from Ref. [74], © Academic Press 1997.

electrical conductivity of mixed electronic-ionic conducting perovskite oxides [78]. However, oxide ion conductivity of $La_2NiO_{4\pm\delta}$ in the intermediate temperature range is higher than that of mixed electronic–ionic conducting perovskite oxides. Skinner and Kilner [79] have shown that oxide ion conductivity is higher in $La_2NiO_{4+\delta}$ than conductivity of $La_{0.6}Sr_{0.4}Co_{0.2}Fe_{0.8}O_3$ (LSCF), but, one order lower than the best perovskite oxide ion conductor $La_{0.3}Sr_{0.7}CoO_3$ (LSC) perovskite. Most of the undoped A_2BO_4 layered perovskites are poor oxide ion conductor due to less oxygen vacancies and interstitial oxide ions [80]. As discussed in Section 2, on partial substitution the oxygen stoichiometry tunes, i.e., material either becomes hypo-stoichiometric or hyper-stoichiometric [39,81]. Oxygen vacancies in the structure provide necessary pathways for oxide ion migration via hopping through the vacant sites [82]. Generally, on acceptor substitution A_2BO_4 layered perovskites becomes hypo-stoichiometric. But, sometimes even after substituting acceptor ions structure is hyper-stoichiometric. This is because of excess number of interstitial oxide ions than the oxygen vacancies in structure. The interstitial oxide ions also migrate in the structure and contribute to the oxide ion conductivity. Some of acceptor substituted hyper-stoichiometric structures show high mixed ionic and electronic conductivity [79]. The substitution of acceptor cations at A-site also promotes the oxidation of B-cation, according to Eq. (10). Partial oxidation of B-cation enhances the electrical conductivity. Electron bounded with unoxidized B-cation hops to neighboring oxidized B-cation. During this hopping process, the unoxidized B-cation oxidizes and oxidized B-cation reduces and becomes unoxidized. Similarly, hole bounded with oxidized B-cation hops to neighboring unoxidized B-cation, and during this hopping process, the oxidized B-cation reduces and unoxidized B-cation oxidizes. Sometimes these hopping processes, also produce a lattice distortion on local level at reducing and oxidizing B-cation sites, due to Jahn–Teller (JT) effect [39,83,84]. Thus, the hopping of electron/hole between the reduced and unreduced B-cation is different from the conduction of electron in metals and conduction of electron/hole in semiconductors. In some materials, local lattice distortion and electron/hole make a bound pair with each other (known as polaron), and conduction of these bound pair is known as polaronic conduction [19,85,86]. Further, when two polarons get closer and

bound with each other to minimize their energy by sharing distortion with each other is known as bound bipolaron. Strongly bounded bipolarons are small in size and have integer spin, and thus, have bosonic properties. Formation of bipolarons without sharing distortion with each other is possible by Bose–Einstein condensation mechanism. This might be a possible mechanism for high-temperature superconductivity. The theme of this article makes this discussion out of the scope of this article.

There are various factors on which oxide ion conductivity in these oxides depends. Some of them are oxygen stoichiometry, temperature, oxygen partial pressure, mobility, etc. The dependence of oxide ion conductivity (σ) on temperature is represented by the Arrhenius relationship, given as follows [87]:

$$\sigma T = A \exp\left(-\frac{E_a}{kT}\right) \tag{11}$$

where A and E_a is a pre-exponential factor and activation energy of oxide ion migration, respectively. In Table 1, the values of activation energy and highest value of electrical conductivity (measured experimentally) along with their references are listed. In these studies migration of oxide ions have been emphasized. For example, in $La_{2-x}Sr_xCuO_4$ the activation energy of oxygen diffusion decreases with increasing concentration of Sr upto $x \leq 0.7$, and after that increases for $0.7 < x \leq 2.0$. The increase in the value of activation energy is explained in terms of immobilization of oxygen vacancy due to cluster formation of defects with Cu or ordering of oxygen sublattices [88]. Bochkov *et al.* [89] studied on $La_2Co_xCu_{1-x}O_4$ solid solution and suggested that increasing Co at Cu increases the oxygen content and decreases the electronic conductivity. Oxygen permeation flux also increases with increasing Co concentration for $0.02 \leq x \leq 10$, and after that decreases with further increase in Co concentration, indicates the participation of interstitial oxide ions in oxide ion conduction. The dependence of oxide ion conduction on membrane thickness emphasized the role of surface exchange rates. Oxide ion diffusion is expected to occur via the interstitial oxygen migration mechanism. But, the oxygen permeability studies in $La_2Ni_{0.98}Fe_{0.02}O_{4+\delta}$ and $La_2Ni_{0.88}Fe_{0.02}Cu_{0.10}O_{4+\delta}$ by Kharton *et al.* [90] demonstrated that both interstitial migration and vacancy diffusion mechanisms are contributing in total ionic conductivity.

It is noted that both oxygen hyper-stoichiometric ($A_2BO_{4+\delta}$) and hypo-stoichiometric ($A_2BO_{4-\delta}$) oxides consist oxygen vacancies, $V_o^{\bullet\bullet}$ and oxide ions, O_i'' as defects. Consequently, in these materials oxide ion conductivity is mediated by both oxygen vacancies and interstitial oxide ions. Therefore, the diffusion coefficient of oxygen is given as [91]:

$$D_o = D_V[V_o^{\bullet\bullet}] + D_i[O_i''] \tag{12}$$

where D_V and D_i are diffusion coefficient of oxygen vacancy and interstitial oxide ion, respectively. Whereas, $[V_o^{\bullet\bullet}]$ and $[O_i'']$ represent concentration of oxygen vacancy and interstitial oxide ion, respectively. The oxygen diffusion in these materials is anisotropic in nature. Molecular dynamics (MD) studies of oxide ion conduction in $La_{1.63}Sr_{0.37}CuO_{3.81}$ and $LaSrCuO_{3.5}$ showed that the mobility of oxygen species in $La(Sr)_2O_2$ bilayers and CuO_2 is significantly different and later being more favored for oxide ion conduction [92,93]. Opila *et al.* [88] have reported the anisotropic nature of oxygen diffusion in ab-plane (basal plane) and along c-axis in $La_{2-x}Sr_xCuO_4$. Atomistic computer simulation of oxide ion conduction mechanisms in tetragonal La_2NiO_4 was done by Cleave *et al.* In this study, a number of vacancy pathways within the *ab*-plane and along the *c*-axis were considered. Interstitial migration of oxide ion according to interstitial migration mechanism was also considered. This study showed that the activation energy for oxide ion migration via vacancies is lower than the activation energy for migration of oxide ions via interstitial sites. In vacancy mechanism the activation energy for oxide ion migration within the ab-plane among equatorial sites is 0.55 eV and via apical sites is only 0.35 eV. And, if an oxide ion moves from equatorial site to a vacant site at apical site it has to overcome an energy barrier of 0.77 eV. Whereas, in interstitial migration mechanism oxide ion has to overcome an energy barrier of 0.86 eV for their migration in ab-plane [82]. Chroneos *et al.* [94] investigated the conduction pathways of interstitial oxide ions and vacancies in stoichiometric tetragonal La_2NiO_4 by MD simulation method. This study also shows that the vacancy migration mechanism in ab-plane is a most favorable mechanism of the oxide ion conduction with the migration activation energy of 0.51 eV in a temperature range of $500 - 800$ ℃. Oxygen stoichiometry does not affect activation energy very significantly. Experimental studies on polycrystalline La_2NiO_4 by Sayers *et al.* [95] predicted that the activation energy for oxygen migration is 0.54 eV. This is consistent with the most recent MD studies by Chroneos *et al.* [94].

4 Dielectric properties

4. 1 Giant (colossal) dielectric materials

The discovery of very high dielectric constant ($\varepsilon_r \approx 10^4$ at 300 K) first in $CaCu_3Ti_4O_{12}$ (CCTO) and later in compounds such as $AFe_{0.5}B_{0.5}O_3$ ($A = Ba, Sr, Ca$; $B = Nb, Ta, Sb$), $Gd_{0.6}Y_{0.4}BaCo_2O_{5.5}$, $La_{0.5}Sr_{0.5}Ga_{0.6}Ti_{0.4}O_{3-\delta}$ increased the interest of researchers towards investigation of dielectric properties of RP phase oxides including A_2BO_4 oxides [114–117]. Although, in recent years La_2NiO_4 has been widely investigated for its mixed ionic and electronic conducting (MIECs) properties useful for SOFCs. But dielectric properties of doped and undoped La_2NiO_4 oxides have also been investigated due to their very large (giant/colossal) value of the dielectric constant in the wide range of temperature and frequency. Due to high value of dielectric constant these oxides have immense potential for their applications in modern microelectronics and for the development of capacitor-based energy storage devices [118].

Till date the origin of colossal dielectric constant (CDC) is highly debated. Many authors, as Lunkenheimer *et al.*, Sinclair *et al.*, and Cohen *et al.* assigned the origin of CDC to extrinsic effects, i.e., to Maxwell–Wagner (MW) interfacial polarization at sample–electrode/grain–grain boundary interfaces [114,119–121]. Interfacial polarization or space charge polarization occurs when conducting charge carriers traveling within the grains get pile up at grain–grain boundary interfaces due to insulating nature of grain boundaries. However, some authors claim that intrinsic effect, i.e., small polaronic hopping and hence charge ordering is responsible for the colossal dielectric constant (CDC) [122–124]. There is also another group of authors, who believe that both intrinsic as well as extrinsic effects are responsible for CDC in different range of temperature and frequencies [17,124–126]. Dielectric properties of La_2NiO_4 oxide have been further modified by substituting different alkaline earth metals (Ca, Sr, and Ba) at La site. Chouket *et al.* [124] studied $LaSrNiO_4$, and reported dielectric relaxation phenomenon. They attributed dielectric relaxation phenomenon to small polaronic hopping process due to closeness of activation energies of relaxation time and bulk electrical conduction. However, a large difference in activation energies of bulk and grain boundaries electrical conduction confirmed the existence of the MW effect in the ceramic. In another studies on Mn-substituted $LaSrNi_{1-x}Mn_xO_4$ nickelates, they have reported two dielectric relaxation processes in two different temperature ranges [125]. The relaxation process occurring between 200 and 300 K was attributed to MW polarization due to conducting (grain) and insulating (grain boundary) regions. A weaker relaxation process below 150 K was ascribed to charge ordering. Equivalence in activation energies of low temperature and high frequency dielectric relaxation time and bulk electrical conductivity calculated according to small polaronic model confirms the role of adiabatic small polaronic hopping process in dielectric relaxation. Song *et al.* have studied dielectric properties of $La_{1.75}Ba_{0.25}NiO_4$ ceramics prepared by spark plasma sintering (SPS) process. In this oxide also two dielectric relaxation processes were observed. The lower temperature relaxation process was credited to the charge ordering and high temperature one to the Maxwell–Wagner polarization. Although the dielectric loss of $La_{1.75}Ba_{0.25}NiO_4$ is lower than that of some Sr substituted nickelate ceramics, but still it is not suitable for the practical applications due to high dielectric loss [127]. Shi *et al.* [128] have reported colossal dielectric properties in $La_{2-x}Ca_xNiO_{4+\delta}$. Among all the samples, at 1 MHz $La_{1.8}Ca_{0.2}NiO_{4+\delta}$ has the highest value of dielectric constant ($\varepsilon_r = 5103$) whereas $La_{1.7}Ca_{0.3}NiO_{4+\delta}$ has the lowest loss. Doping of Ca effectively increases the ε_r and reduces the dielectric loss. Fan *et al.* [21] tried to explain the dielectric loss from the relationship of two polar-phonon modes and structure. According to their theory, dielectric loss is influenced by $(La, Ca)-O(1)$, $(La, Ca)-O(2a)$, and $(La, Ca)-O(2b)$ bonds and if the normalized values of any cation–oxygen bond approach 1, the dielectric loss attains its minimum value. From $La_2NiO_{4+\delta}$ to $La_{1.7}Ca_{0.3}NiO_{4+\delta}$, normalized bond valences of $Ca-O(1)$, $Ca-O(2a)$, and $La-O(2a)$ approach 1, reducing the dielectric loss greatly. In Ca doped La_2NiO_4 $La-O(2b)$ and $Ca-O(2b)$ bonds are heavily compressed; this may be the reason for high dielectric loss. Among all prepared compositions, the minimum elongation of $Ca-O(1)$, $Ca-O(2a)$, and $La-O(2a)$ bonds was observed in $La_{1.7}Ca_{0.3}NiO_{4+\delta}$ causing lowest dielectric loss for this particular composition. A detailed dielectric investigation on charge ordered $La_{15/8}Sr_{1/8}NiO_4$ upto 1 GHz frequency have been carried by Krohns *et al.* [129]. They reported that this sample retains its colossal dielectric constant well into the technically required gigahertz frequency range. The

dielectric properties of $La_{15/8}\,Sr_{1/8}NiO_4$ are superior to other colossal dielectric materials, including most investigated $CaCu_3Ti_4O_{12}$ (CCTO). Wang *et al.* [126] studied dielectric properties of the $A_{5/3}Sr_{1/3}Ni_{1-x}Al_xO_4$ $(A = La, Nd;\ x = 0.2, 0.3)$ solid solution. They ascribed giant dielectric response of composition with $x = 0.3$ to the adiabatic small polaronic hopping process, because the value of activation energy of dielectric relaxation and bulk electrical conduction is very close. However, in the composition with $x = 0.2$, both dielectric relaxations were observed, attributed to adiabatic small polaronic hopping process and MW effect. In all the above-mentioned studies on dielectric properties of undoped, doped, and co-doped La_2NiO_4 oxides, low temperature (< 150 K) dielectric relaxation process is attributed to small polaronic hopping mechanism based on the closeness of activation energy values of bulk conductivity and dielectric relaxation. Similarly, high temperature (> 150 K) dielectric relaxation process is ascribed to Maxwell–Wagner polarization based on the closeness of activation energy values of grain boundaries conduction and high-temperature dielectric relaxation.

The contribution of oxygen vacancy in the giant dielectric constant of $Sm_{1.5}Sr_{0.5}NiO_{4-\delta}$ has been studied by Liu *et al.* [130]. The giant dielectric response in as-sintered $Sm_{1.5}Sr_{0.5}NiO_{4-\delta}$ ceramic is directly linked to the small polaronic hopping process, while in the annealed sample it is linked to oxygen vacancy concentrations. Annealing in a nitrogen gas atmosphere increases the oxygen vacancies in $Sm_{1.5}Sr_{0.5}NiO_{4-\delta}$, and consequently, the dielectric constant at low temperature is decreased and increased at high temperature. However, the dielectric loss is increased in the overall temperature range. Dielectric studies in oxygen hyper-stoichiometric $Nd_2NiO_{4+\delta}$ ceramic by Liu *et al.* [19] confirmed the similar mechanism of dielectric relaxation. In hyper-stoichiometric ceramics, excess holes are generated in the structure according to Eq. (2), as mentioned in Section 2. As the content of excess oxygen decreases the concentration of excess holes also decreases and hence the activation energy of dielectric relaxation at low temperature increases. These studies reveal that the dielectric properties of A_2BO_4 strongly depends on oxygen stoichiometry.

Jia *et al.* [16] studied the effect of polaronic concentration on dielectric properties of Mn-substituted $Sm_{1.5}Sr_{0.5}NiO_4$ ceramics. They have reported that the dielectric loss decreases with increasing content of Mn ions at Ni sites. At low temperature, on increasing content of Mn ions at Ni sites polaron concentration decreases and its size increases leading to increase in the value of dielectric constant and decrease in the dielectric loss. The change in the microstructure of $La_{1.5}Sr_{0.5}Ni_{1-x}Ga_xO_4$ ceramic as a function of concentration of Ga^{3+} has been carried out. The substitution of Ga^{3+} in $La_{1.5}Sr_{0.5}Ni_{1-x}Ga_xO_4 (x = 0, 0.1, 0.3)$ has remarkably influenced the microstructure and increased the value of total resistance [131]. Due to increase in the value of resistance of $La_{1.5}Sr_{0.5}Ni_{1-x}Ga_xO_4$, its dielectric constant has increased and loss has decreased significantly.

The studies of $La_{1.5}Sr_{0.5}Ni_{1-x}Ga_xO_4$ also highlighted the effect of sample electrode interface polarization on the dielectric properties. The effect of DC bias on non-ohmic sample–electrode contact and grain boundary responses were studied in Mg substituted $La_{1.7}Sr_{0.3}Ni_{1-x}Mg_xO_4$ ceramics by Meeporn *et al.* [43]. For undoped $La_{1.7}Sr_{0.3}NiO_4$, capacitance "C" decreases with increasing DC bias voltage and follows the Mott–Schottky law which confirmed the effect of sample electrode interface on the dielectric properties. However, for Mg substituted $La_{1.7}Sr_{0.3}Ni_{1-x}Mg_xO_4$ the decrease in "C" values with increasing DC bias voltage does not follow the Mott–Schottky law, indicating negligible contribution of sample electrode interface polarization. This decrease in capacitance "C" is attributed to significant increase in the resistance of grain boundaries on Mg substitution.

The dielectric properties of manganite A_2BO_4 oxides were also studied. In $Sr_2Mn_{0.5}Ti_{0.5}O_4$ only one high temperature (above 453 K) dielectric relaxation is present, which is attributed to the MW polarization. The low-temperature dielectric relaxation generally originated from adiabatic small polaronic hopping process is absent in $Sr_2Mn_{0.5}Ti_{0.5}O_4$. It was observed that in $Sr_2Mn_{0.5}Ti_{0.5}O_4$ both titanium and manganese ions are in "4+" oxidation state that is why the concentration of oxygen vacancies and polarons in the unit cell are almost zero [132]. It is important to notice here that the dielectric constant of $Sr_2Mn_{0.5}Ti_{0.5}O_4$ is not as high as of doped and co-doped La_2NiO_4. This is because degree of polyhedral distortions in $Sr_2Mn_{0.5}Ti_{0.5}O_4$ is much less as compared with doped/co-doped La_2NiO_4. Further, it is observed that when all the "B" cation are in the same oxidation state, the distortion in the polyhedra is minimum and charge ordering is absent. This results in lowering dielectric

constant values. The effect of charge ordering has been studied in Pr doped $Ca_{2-x}Pr_xMnO_4$. Undoped Ca_2MnO_4 does not show charge-order, and the measured intrinsic dielectric constant is only 14. The Pr doping induces charge-order in the system causing noteworthy increase in the value of dielectric constant, ε_r ($\sim$220) for $Ca_{1.75}Pr_{0.25}MnO_4$ [133].

4. 2 Microwave dielectric materials

There is also another group of A_2BO_4 layered perovskites, which have been studied for low-loss microwave dielectric applications. The general formula for these ceramics is $MLnBO_4$ ($M = Ca, Sr, Ba; Ln = Y, La, Nd, Sm; B = Al, Ga, (Mg_{0.5}Ti_{0.5}), (Zn_{0.5}Ti_{0.5})$) [134]. Among these oxides, $CaLaAlO_4$ and $SrYAlO_4$ are not stable. This is because, for these two oxides the difference between tolerance factor "t" of layered perovskite and its perovskite unit (i.e., $LaAlO_3$ in $CaLaAlO_4$, and $YAlO_3$ in $SrYAlO_4$) is greater than 4.3%. Stability of $CaLaAlO_4$ has been improved by substituting Sr at Ca, in $Ca_{1-x}Sr_xLaAlO_4$ stability is reported for composition with $x > 0.9$ [135]. In the crystal structure of $MLnBO_4$, large distortion in $(M, Ln)O_9$ polyhedra and BO_6 octahedra are observed in the crystal structure. These distortions originate due to a large difference in the ionic radii of M and Ln cations, also leading to an interlayer size mismatch. Between these interlayers static electric polarization may also be present due to "2+" oxidation state of cation M and "3+" oxidation state of cation Ln (discussed in detail in Section 2) [21,134,136,137]. There are several studies in which improvement in $Q \times f$ ($Q = \frac{\varepsilon'}{\varepsilon''} = \frac{1}{\tan\delta}$ and $f =$ frequency) has been achieved by reducing interlayer static electric polarization [21,136,138,139]. The solid solution of $SrLaAlO_4, SrNdAlO_4, SrSmAlO_4, CaNdAlO_4$ with Sr_2TiO_4/Ca_2TiO_4 (i.e., $Sr_{1+x}La_{1-x}Al_{1-x}Ti_xO_4$, $Sr_{1+x}Nd_{1-x}Al_{1-x}Ti_xO_4$, $Sr_{1+x}Sm_{1-x}Al_{1-x}Ti_xO_4$, $Ca_{1+x}Nd_{1-x}Al_{1-x}Ti_xO_4$, respectively) have been extensively studied by several research groups and improvement in $Q \times f$ were reported by co-substitution of Sr(Ca)/Ti cations. Co-substitution reduces the interlayer polarization and results in improving $Q \times f$ value. Co-substitution also decreases the tolerance factor "t" and subsequently interlayer stress increases. Sometimes a new phase $MTiO_3$ also appears. These two effects: decrement in tolerance factor "t" and appearance of the new phase, bring a negative impact on $Q \times f$ improvement [24,136–140]. Although $MLnAlO_4$ ceramics have high $Q \times f$ values ($\sim$ 90000 GHz) and further improvement in $Q \times f$ values is also observed in solid solution with Sr_2TiO_4/Ca_2TiO_4. But, relatively low dielectric constant ($\varepsilon_r \sim 20$) and higher temperature coefficient of the resonant frequency τ_f (~ -30 ppm/℃) limit their practical applications. The improvement in ε_r was expected by replacing Al^{3+} with suitable trivalent cation having ionic polarizability higher than 0.78 Å^3 of Al^{3+} cation. However, only Ga^{3+} is found to be a suitable cation with ionic polarizability of 1.50 Å^3, by considering the stability of A_2BO_4 layered perovskite structure and electrically insulator (an essential requirement for microwave dielectric ceramics). $SrLaGaO_4$ ceramic has higher dielectric constant ($\varepsilon_r = 20.3$) than $SrLaAlO_4$ ($\varepsilon_r = 17.6$) but lower $Q \times f$ value (16200 GHz) than 95200 GHz of $SrLaAlO_4$. The τ_f of $SrLaGaO_4$ is -33.5 ppm/℃ nearly the same as -32 ppm/℃ of $SrLaAlO_4$. The $Q \times f$ value of single crystal $SrLaGaO_4$ is significantly higher 170000 GHz in comparison to $Q \times f$ value of its ceramic 16200 GHz. It was expected to replace Al^{3+} cation by aliovalent cations such as $(Mg_{0.5}Ti_{0.5})^{3+}$ or $(Zn_{0.5}Ti_{0.5})^{3+}$, which have effectively higher ionic polarizability of 2.135 and 2.515 Å^3, respectively. Significant improvement in the dielectric constant was observed in $SrLa(Mg_{0.5}Ti_{0.5})O_4$ ($\varepsilon_r = 25.5$) and $SrLa(Zn_{0.5}Ti_{0.5})O_4$ ($\varepsilon_r = 29.4$) ceramics compared to the analogs $SrLaAlO_4$ and $SrLaGaO_4$, which is attributed to the increased normalized bond lengths of $(Sr/La) - O_{ap}$ and $(Sr/La) - O_{bs}$ and the higher polarizability of $(R_{0.5}Ti_{0.5})^{3+}$ than Al^{3+} and Ga^{3+}. In addition, τ_f also becomes positive (29 ppm/℃ for $SrLa(Mg_{0.5}Ti_{0.5})O_4$ and 38 ppm/℃ for $SrLa(Zn_{0.5}Ti_{0.5})O_4$) with increase in dielectric constant [134]. Although, for these ceramics, the dielectric constant is high but higher τ_f value limits its practical application in commercial microwave devices, such as dielectric resonators and filters [141]. Recently, Sr_2TiO_4 and Sr_2CeO_4 were also studied for low loss microwave dielectric applications by Liu *et al.* and Dai *et al.*, respectively. The dielectric properties of these two ceramics are $\varepsilon_r = 42, Q \times f = 145200$ GHz, $\tau_f = 130$ ppm/℃ for Sr_2TiO_4 and $\varepsilon_r = 14.8$, $Q \times f = 172600$ GHz, $\tau_f = -62$ ppm/℃ for Sr_2CeO_4 [20,142]. High values of $\varepsilon_r, Q \times f$, and τ_f of Sr_2TiO_4, make it suitable for wireless passive temperature sensors application [141]. Properties

of the solid solution of these two oxides have been also studied by Dai *et al.* For $Sr_2Ce_{0.65}Ti_{0.35}O_4$ ($\varepsilon_r = 20.7, Q \times f = 115550$ GHz) very small value of $\tau_f(= -1.8$ ppm/℃) was reported [20]. The microwave dielectric properties of some recently studied A_2BO_4 oxides with respective references are listed in Table 2. A systematic improvement in low-loss microwave dielectric properties is obvious from Table 2.

Till date, no report is found in the literature on experimental measurements to claim ferroelectric characteristics in A_2BO_4 layered perovskites. Although theoretical group of researchers have suggested certain compositional and structural modifications to induce highly improper ferroelectricity (HIF) in RP oxides. On the basis of group theory, they have shown that the condensation of two distortion modes; (i) unique symmetric octahedral distortions (Fig. 6) and (ii) a combination of a single octahedral distortion with "compositional" A- or B-cation ordering (Fig. 7), can transform the centrosymmetric structure into a non-centrosymmetric structure (necessary requirement for a crystal to exhibit ferroelectricity) [143,144]. The general rule that a unique symmetric octahedral distortion for ferroelectric nature, failed to induce HIF in A_2BO_4 layered perovskite as there are an even

Table 2 Dielectric properties of some recently studied ceramics for low-loss microwave applications

Ceramic	ε_r	$Q \times f$(GHz)	τ_f(ppm/℃)	Reference
$CaNdAlO_4$	18.2	17980	−79	[146]
$CaSmAlO_4$	18.2	51060	−3	[146]
$CaYAlO_4$	18.9	39960	6	[146]
$SrSmAlO_4$	18.3	70000	−1	[21]
$SrNdAlO_4$	18.4	55300	−15	[21]
$SrLaAlO_4$	17.6	65500	−32	[21]
$SrLaGaO_4$	20.3	16219	−33.5	[147]
$SrNdGaO_4$	21.4	16650	7.1	[147]
$(Ca_{0.05}Sr_{0.95})LaAlO_4$	16.7	28171	−52.4	[135]
$SrLa(Mg_{0.5}Ti_{0.5})O_4$	25.5	72000	29	[134]
$SrLa(Zn_{0.5}Ti_{0.5})O_4$	29.4	34000	38	[134]
$SrLa[Al_{0.35}(Mg_{0.5}Ti_{0.5})_{0.65}]O_4$	22.2	89,100	−0.1	[23]
$SrLa[Al_{0.5}(Zn_{0.5}Ti_{0.5})_{0.5}]O_4$	23.5	102000	−3.4	[22]
$Ca_{1.15}Nd_{0.85}Al_{0.85}Ti_{0.15}O_4$	19.5	93400	−2	[139]
$Sr_{1.6}Nd_{0.4}Al_{0.4}Ti_{0.6}O_4$	23.6	86300	10.9	[138]
$Sr_{1.4}La_{0.6}Al_{0.6}Ti_{0.4}O_4$	18.5	95000	−8.9	[24]
Sr_2TiO_4	42	145200	130	[142]
Sr_2CeO_4	14.8	172600	−62	[20]
$Sr_2Ce_{0.65}Ti_{0.35}O_4$	20.7	115550	−1.8	[20]

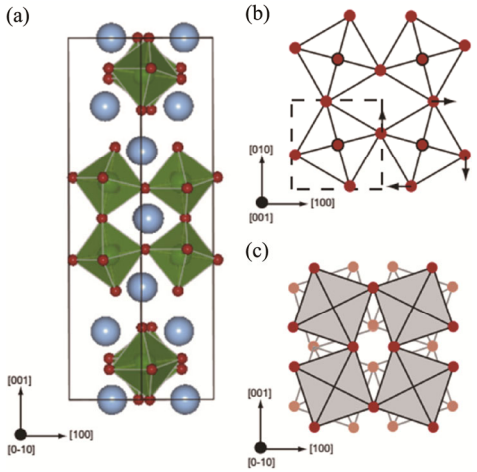

Fig. 6 (a) The $A2_1am$ ferroelectric ground state structure of $Ca_3Ti_2O_7$ and $Ca_3Mn_2O_7$. Large (blue) spheres correspond to Ca ions. (b) Schematic of the atomic displacements corresponding to the X_2^+ rotation mode. The dashed square denotes the unit cell of the $I4/mmm$ reference structure. (c) Schematic of the X_3^- rotation mode. All axes refer to the coordinate system of the $I4/mmm$ reference structure. Reproduced with permission from Ref. [144], © Elsevier Inc. 2012.

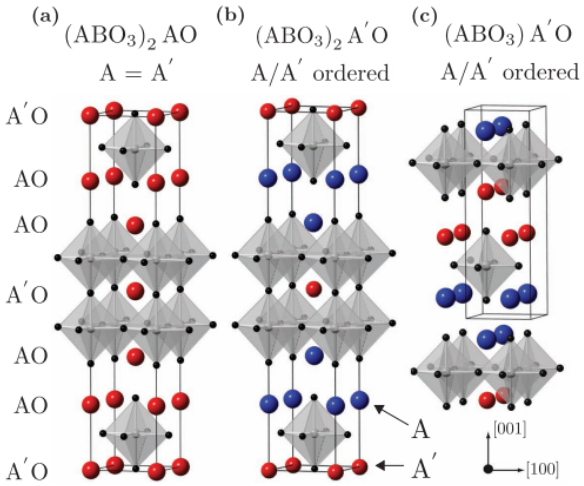

Fig. 7 (a) The $n = 2$ Ruddlesden–Popper structure (without octahedral rotations) with a single A-cation. (b) A/A′ ordered $n = 2$ phase. (c) A/A′ ordered $n = 1$ phase. Reproduced with permission from Ref. [145], © WILEY−VCH Verlag GmbH & Co. KGaA, Weinheim 2013.

number of "A" cations per unit cell. However, symmetrical ordering of "A" cations in $(ABO_3)A'O$ layered perovskite can induce ferroelectricity [145]. The relative magnetoelectric properties corresponding to HIF is also explored in ABO_3 and $A_3B_2O_7$. However, till date it is not explored yet in A_2BO_4 layered perovskites [144].

5 Optical properties

In recent years commercialization of white light-emitting diodes (WLEDs), flat-panel displays, plasma display panels (PDPs), field emission displays (FEDs), and thin-film electroluminescent devices (TFELs) could be possible due to the development of new phosphor materials with improved optical properties [29,148–150]. For the development of new phosphor materials, the efforts to discover new host materials and high-performance activators are needed [29]. Traditionally sulfide and halide phosphors were extensively studied but in recent years oxide phosphors have received attention of the researchers due to their stability [29,150,151]. In A_2BO_4 layered perovskite family, M_2SnO_4 ($M = Ca, Sr, Ba$), Sr_2CeO_4, etc. have been extensively studied as host matrix for phosphor applications because of their stable crystal structure, non-toxicity, and lack of radioactive elements [29]. The incorporation of optically active lanthanide ions into these host matrices results in phosphors with photoluminescence (PL) and long-lasting phosphorescence (LLP) properties [151–153]. The LLP phosphors emitting in the blue and green spectral region are being used in many commercially available optical devices. However, LLP phosphors having emission in orange to red region are still out of reach for the use in optical devices. Therefore, there is need for the development of novel host materials for LLP phosphors emitting light in the orange to red wavelength range [29,153]. The properties of LLP phosphor have been modified by using a host-mixing method to change the original constituents of the lattice or introducing different co-dopant [29]. Important performance factors are bandgap, energy gap between excited states and the conduction band, and energy states corresponding to defects and their density. The luminous color of the WLED depends on the emission center used in the phosphors. The red and orange emission of phosphor mainly derives from the electron transition of the internal orbit of Sm^{3+} and Eu^{3+}. The Sm^{3+} (electron configuration $4f^5$) and Eu^{3+} (electron configuration $4f^6$) ions have incomplete 4f shell, and their outer $5s^2$ and $5p^6$ orbits shield 4f electrons against the crystal field [29,154]. Therefore, the optical spectra of Sm^{3+} and Eu^{3+} in the crystal lattice are fairly similar to the free ions and show good color purity. Kamimura *et al.* [155] reported the purple photochromism in Eu^{3+} doped Sr_2SnO_4. The incorporation of Ti^{4+} in alkaline earth orthostannates (M_2SnO_4) was studied for blue photoluminescence applications. According to Yamashita *et al.*, the excitation spectra of these orthostannates exhibited broad bands just below the fundamental absorption edges, implying that luminescence centers do not consist of the component elements in the host materials. It was suggested that the Ti containing octahedra are possible luminescence centers in these materials, as it was proposed for earlier investigated Ti-doped Mg_2SnO_4 and $Y_2Sn_2O_7$ [150,156].

Another phosphor which has drawn wide attention of researchers in recent years for its optical properties is Sr_2CeO_4, firstly reported by Danielson and his co-workers in 1998 [157]. It is intrinsically luminescent material and has chemically and thermal stability. Sr_2CeO_4 also possesses some desirable qualities of phosphor materials such as (i) ligands-to-metal charge transfer (CT) transition of Ce^{4+} at ~340 nm, (ii) efficient energy transfer that can occur from the $Ce^{4+}-O^{2-}$ CT state to the trivalent rare earth in $Sr_2CeO_4:RE^{3+}$, (iii) high efficiency for absorbing UV radiation, and (iv) the large band gap [40]. Almost all cerium-based phosphors are known due to their localized Ce^{3+} excited state with luminescence arising from 4f to 5d transitions. However, in Sr_2CeO_4 the cerium ion is in "4 +" oxidation state and the 4f shell is empty, the only possible transition is metal to ligand charge transfer transition originating due to the interaction of central cerium ion with neighboring oxygen ligands in CeO_6 octahedra [158]. Figure 8(a) shows the photoluminescence excitation (PLE) spectra of Sr_2CeO_4 phosphor. The excitation spectra consist of a broad spectrum in UV-region between 200 and 400 nm with a peak at 299 nm and a shoulder at 349 nm. The broadness of the excitation spectrum indicates the possibilities of using Sr_2CeO_4 phosphor in UV LED chips. Two peaks in the excitation spectra of Sr_2CeO_4 are associated with two different $Ce^{4+}-O^{2-}$ bond-lengths. The excitation from the ground state to the excited states is attributed to the $t_{1g}-f$ (terminal) and $t_{1u}-f$ (equatorial) charge transfer states of Ce^{4+}. The band $t_{1u}-f$ is spin forbidden; hence the excitation intensity associated with it is lowered than the band associated with $t_{1g}-f$ state [158]. Therefore, the higher energy band (299 nm) originates from charge transfer from apical oxygen, O_{ap} to Ce^{4+} and lower energy band (349 nm) originates from the charge transfer from equatorial oxygen, O_{eq} to Ce^{4+}. Figure 8(b) shows photo-luminescence

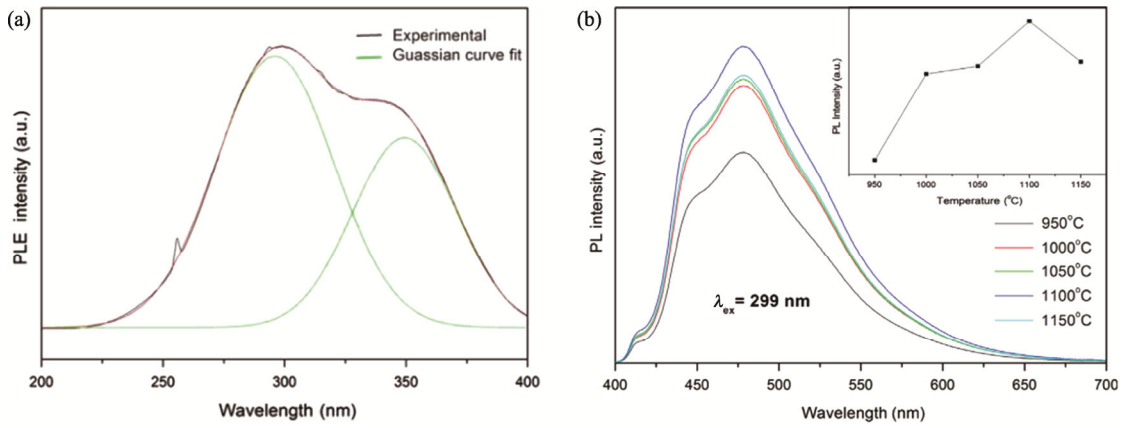

Fig. 8 (a) Excitation spectra of Sr_2CeO_4 phosphor with a Gaussian fit. (b) The emission spectra of Sr_2CeO_4 phosphor sintered at various temperature from 950 to 1150 ℃ under the excitation wavelength at 299 nm. Reproduced with permission from Ref. [158], © Elsevier Ltd and Techna Group S.r.l. 2014.

emission spectra of Sr_2CeO_4 under the excitation wavelength at 299 nm. The emission spectrum shows board band emission (FWHM ≈ 100 nm) in blue region with a maximum at 478 nm via radiative transition from the excited charge transfer state to the ground state [158].

The improvement in the emission intensity of Sr_2CeO_4 has been achieved by increasing sintering temperature as plotted in the inset of Fig. 8(b). It is mentioned that with increasing sintering temperature crystallinity improves, and hence emission intensity increases up to 1100 ℃. Above 1100 ℃ no further improvement in the crystallinity could be achieved due to high agglomeration at a higher temperature, and hence emission intensity starts decreasing. The Commission International De I-Eclairage (CIE) chromaticity coordinates of the Sr_2CeO_4 phosphors sintering at different temperatures lie in the blue region.

In recent years rare earth (RE^{3+}) ions such as Eu^{3+}, Ho^{3+}, Er^{3+}, Tm^{3+}, Dy^{3+}, Yb^{3+} etc. doped Sr_2CeO_4 phosphors have attracted lots of attention from the researchers [148]. $Sr_2CeO_4:Eu^{3+}$ (Dy^{3+}, Tm^{3+}) phosphors have exhibited strong red (yellow, blue) emission which makes them potential for display applications such as UV-LEDs [159]. Rare earth ions (Ho^{3+}, Er^{3+}, Tm^{3+}, and Yb^{3+}) doped Sr_2CeO_4 phosphors have been studied for their application as lasing materials or spectral conversion materials [159]. Dy^{3+} doped phosphors have shown two intense emission at 484 nm (blue) and 575 nm (yellow) useful for white light emission based optical devices. However, these emission lines (of Dy^{3+}) are very sensitive to the chemical environment surrounding the luminophore. The intensity ratios of these two emission bands are host dependent. Therefore, emission of white light can be realized by modulating the intensity of emission, i.e., by compositional modification of the host [40]. In Eu^{3+} and Dy^{3+} co-doped Sr_2CeO_4, the photoluminescence mechanism of energy transfer between Eu^{3+} and Dy^{3+} for color tunable phosphor applications has been studied by Li *et al*. [157]. They also studied the energy transfer between $Ce^{4+}-O^{2-}$ charge-transfer state (CTS) and Eu^{3+} states by theoretical calculation of the band structure. They found that the efficiency of co-doped phosphors is lowered as compared to single ion doped phosphors due to the reabsorption mechanism between the Eu^{3+} and Dy^{3+} co-dopants. $Sr_2CeO_4:Nd^{3+}$ nanophosphors exhibit a strong near-infrared (NIR) emission and can be used as high-efficiency laser material based on their peculiar optical properties [157].

Recent research reports have emphasized the role of co-doping of alkali metal ions (Li^+, Na^+, K^+) along with rare-earth ions (RE^{3+}) in some of A_2BO_4 oxides. This approach has been employed in several phosphors, like $CaMO_4:Dy^{3+}$ (M = W, Mo), $Y_2Zr_2O_7:Dy^{3+}$, $YBO_3:Eu^{3+}$, $YPO_4:Eu^{3+}$, etc. [160–163]. The co-doping of monovalent alkali metal ions reduces the charge unbalancing problem originated by doping of trivalent rare-earth ions at divalent alkaline earth metal ions (Ca^{2+}, Sr^{2+}, Br^{2+}). Co-doping of alkali metal ions (Li^+, Na^+, K^+) along with rare-earth ions (RE^{3+}) approach has emerged as an efficient way to enhance the photoluminescence (PL) intensity and emission characteristics of A_2BO_4 oxides based phosphors [40].

6 Conclusions and perspective

Only those A_2BO_4 compounds which crystallize in T-type structure form layered perovskite structure or K_2NiF_4 structure. All the investigated A_2BO_4 layered perovskites have either orthorhombic or tetragonal crystal structure. At high temperature due to the expansion in the unit cell volume of RE_2MO_4 oxides, orthorhombic to tetragonal structural transformation is observed. The structural transformation in these oxides can be induced by varying oxygen stoichiometry and selecting suitable dopants. Both hypo-stoichiometric (less oxygen, $A_2BO_{4-\delta}$) and hyper-stoichiometric (more oxygen, $A_2BO_{4+\delta}$) can be synthesized by changing processing conditions or dopants.

Majority of A_2BO_4 oxides are insulator in nature. However, hypo-/hyper-stoichiometric RE_2MO_4 and AE doped RE_2MO_4 have high value of conductivity due to mixed ionic–electronic conducting properties. Due to a wide range of oxygen stoichiometry and large interstitial space for oxide ion migration, the mixed ion conductivity is higher in La_2NiO_4 making it useful for cathode in IT-SOFCs. Among all the investigated RE_2MO_4, $Pr_{1.3}Sr_{0.7}Ni_{0.7}Cu_{0.3}O_4$ shows the highest ($260\ S\cdot cm^{-1}$ at 700 ℃) mixed ionic–electronic conductivity (MIEC). The stability of Ln_2NiO_4 with commonly used electrolytes in SOFCs has been performed but more studies are needed for practical application.

Recently, some of A_2BO_4 oxides having giant/ colossal dielectric constant were explored. Doped and undoped La_2NiO_4 have shown very large ("giant") magnitude of the dielectric constant and thus display immense potential for their applications in modern microelectronics and for the development of capacitor-based energy storage devices. The dielectric properties of $La_{15/8}Sr_{1/8}NiO_4$ are superior to popular high dielectric constant material $CaCu_3Ti_4O_{12}$ (CCTO). Until now no ferroelectric characteristics have been observed experimentally in any A_2BO_4 layered perovskites. Theoretical researchers have suggested certain compositional and structural modifications to induce highly improper ferroelectricity (HIF) in RP oxides. But the only compositional ordering of "A" cations found suitable in $(ABO_3)A'O$ layered perovskites.

There is also another group of A_2BO_4 layered perovskites which have been studied for low-loss microwave dielectric applications. Very high values of $\varepsilon_r, Q\times f,$ and τ_f of Sr_2TiO_4, make it very suitable for wireless passive temperature sensor application.

The A_2BO_4 layered perovskites have also been studied for phosphor applications. M_2SnO_4 ($M = Ca, Sr, Ba$) and Sr_2CeO_4 are extensively studied as a host matrix because of their wide optical band gap ($3-5$ eV), stable crystal structure, physical and chemical stability, non-toxicity, and lack of radioactive elements. Among all the investigated A_2BO_4 oxides, Sr_2CeO_4 has shown self-luminescence in blue region.

In the last two decades researchers have mainly focused attention on La_2NiO_4, and studies on the properties of other oxides such as A_2BO_4 ($A = Ca, Sr, Ba$ and $B = Sn, Ti, Mn$) are very limited. Dielectric properties of Sr_2SnO_4 and Sr_2MnO_4 investigated by our research group are promising and need more investigations for further improvement. The understanding about the origin of high dielectric constant in La_2NiO_4 is not clear and needs more experimental and theoretical research on this system. Although theoretical researchers have suggested certain compositional and structural modifications to induce HIF in RP oxides, experimentally these modifications are not employed yet.

Acknowledgements

Mr. Gurudeo Nirala and Mr. Dharmendra Yadav are thankful to the Ministry of Human Resource and Development (MHRD), Government of India for the financial support in terms of Senior Research Fellowship (SRF).

References

[1] Ruddlesden SN, Popper P. The compound $Sr_3Ti_2O_7$ and its structure. *Acta Cryst* 1958, **11**: 54–55.

[2] Hirayama T, Nakagawa M, Sumiyama A, *et al*. Superconducting properties in $La_2CuO_{4+\delta}$ with excess oxygen. *Phys Rev B* 1998, **58**: 5856–5861.

[3] Tholence JL. Superconductivity of La_2CuO_4 and $YBa_2Cu_3O_7$. *Phys B+C* 1987, **148**: 353–356.

[4] Suter A, Logvenov G, Boris AV, *et al*. Superconductivity drives magnetism in δ-doped La_2CuO_4. *Phys Rev B* 2018, **97**: 134522.

[5] Bates FE, Eldridge JE. Normal modes of tetragonal La_2NiO_4 and La_2CuO_4, isomorphs of the hight T_c superconductor $La_{2-x}Sr_xCuO_4$. *Solid State Commun* 1989, **72**: 187–190.

[6] Burns G, Dacol FH, Kliche G, *et al*. Raman and infrared studies of Sr_2TiO_4: A material isomorphic to $(La,Sr)_2CuO_4$ superconductors. *Phys Rev B* 1988, **37**: 3381–3388.

[7] Moritomo Y, Asamitsu A, Kuwahara H, *et al*. Giant

magnetoresistance of manganese oxides with a layered perovskite structure. *Nature* 1996, **380**: 141–144.

[8] Wang XL, Takayama-Muromachi E, Dou SX, *et al*. Band structures, magnetic properties, and enhanced magnetoresistance in the high pressure phase of Gd and Y doped two-dimensional perovskite Sr_2CoO_4 compounds. *Appl Phys Lett* 2007, **91**: 062501.

[9] Gebhardt JR, Roy S, Ali N. Colossal magnetoresistance in Ce doped manganese oxides. *J Appl Phys* 1999, **85**: 5390–5392.

[10] Goodrich R, Hall D, Palm E, *et al*. Magnetoresistance below 1 K and temperature cycling of ruthenium oxide–bismuth ruthenate cryogenic thermometers. *Cryogenics* 1998, **38**: 221–225.

[11] Zhu M, Peng J, Zou T, *et al*. Colossal magnetoresistance in a Mott insulator via magnetic field-driven insulator–metal transition. *Phys Rev Lett* 2016, **116**: 216401.

[12] Pikalova E, Sadykov VA, Filonova EA, *et al*. Structure, oxygen transport properties and electrode performance of Ca-substituted Nd_2NiO_4. *Solid State Ionics* 2019, **335**: 53–60.

[13] Chaudhari VN, Khandale AP, Bhoga SS. Sr-doped Sm_2CuO_4 cathode for intermediate temperature solid oxide fuel cells. *Solid State Ionics* 2014, **268**: 140–149.

[14] Kovalevsky AV, Kharton VV, Yaremchenko AA, *et al*. Stability and oxygen transport properties of $Pr_2NiO_{4+\delta}$ ceramics. *J Eur Ceram Soc* 2007, **27**: 4269–4272.

[15] Hyodo J, Tominaga K, Ju YW, *et al*. Electrical conductivity and oxygen diffusivity in Cu- and Ga-doped Pr_2NiO_4. *Solid State Ionics* 2014, **256**: 5–10.

[16] Jia BW, Liu XQ, Chen XM. Structure, magnetic and dielectric properties in Mn-substituted $Sm_{1.5}Sr_{0.5}NiO_4$ ceramics. *J Appl Phys* 2011, **110**: 064110.

[17] Yang WZ, Song CL, Liu XQ, *et al*. Dielectric relaxation and polaronic hopping in the single-layered perovskite $La_{1.5}Sr_{0.5}CoO_4$ ceramics. *J Mater Sci* 2011, **46**: 6339–6343.

[18] Liu XQ, Jia BW, Yang WZ, *et al*. Dielectric relaxation and polaronic hopping in Al-substituted $Sm_{1.5}Sr_{0.5}NiO_4$ ceramics. *J Phys D: Appl Phys* 2010, **43**: 495402.

[19] Liu G, Chen TT, Wang J, *et al*. Effect of excess oxygen on crystal structures and dielectric responses of $Nd_2NiO_{4+\delta}$ ceramics. *J Alloys Compd* 2013, **579**: 502–506.

[20] Dai QL, Zuo RZ. A novel ultralow-loss Sr_2CeO_4 microwave dielectric ceramic and its property modification. *J Eur Ceram Soc* 2019, **39**: 1132–1136.

[21] Fan XC, Chen XM, Liu XQ. Structural dependence of microwave dielectric properties of $SrRAlO_4$ (R = Sm, Nd, La) ceramics: Crystal structure refinement and infrared reflectivity study. *Chem Mater* 2008, **20**: 4092–4098.

[22] Liu B, Li L, Liu XQ, *et al*. Structural evolution of $SrLaAl_{1-x}(Zn_{0.5}Ti_{0.5})_xO_4$ ceramics and effects on their microwave dielectric properties. *J Mater Chem C* 2016, **4**: 4684–4691.

[23] Chen GY, Ren GR, Li L, *et al*. Structure and microwave dielectric properties of $SrLa[Al_{1-x}(Mg_{0.5}Ti_{0.5})_x]O_4$ (x = 0.2–0.8) ceramics. *Ceram Int* 2018, **44**: 1984–1990.

[24] Mao MM, Chen XM, Liu XQ. Structure and microwave dielectric properties of solid solution in $SrLaAlO_4$–Sr_2TiO_4 system. *J Am Ceram Soc* 2011, **94**: 3948–3952.

[25] Chen YC, Chang YH, Tsai BS. Influence of processing conditions on synthesis and photoluminescence of Eu^{3+}-activated strontium stannate phosphors. *J Alloys Compd* 2005, **398**: 256–260.

[26] Sahu M, Gupta SK, Jain D, *et al*. Solid state speciation of uranium and its local structure in Sr_2CeO_4 using photoluminescence spectroscopy. *Spectrochim Acta Part A: Mol Biomol Spectrosc* 2018, **195**: 113–119.

[27] Li J, Li X, Hu SL, *et al*. Photoluminescence mechanisms of color-tunable Sr_2CeO_4:Eu^{3+},Dy^{3+} phosphors based on experimental and first-principles investigation. *Opt Mater* 2013, **35**: 2309–2313.

[28] Gao H, Wang YH. Photoluminescence of Eu^{3+} activated Ba_2SnO_4 under ultraviolet–vacuum ultraviolet excitation. *J Mater Res* 2006, **21**: 1857–1861.

[29] Stanulis A, Katelnikovas A, Enseling D, *et al*. Luminescence properties of Sm^{3+}-doped alkaline earth ortho-stannates. *Opt Mater* 2014, **36**: 1146–1152.

[30] Labhasetwar N, Saravanan G, Kumar Megarajan S, *et al*. Perovskite-type catalytic materials for environmental applications. *Sci Technol Adv Mater* 2015, **16**: 036002.

[31] Schön A, Dujardin C, Dacquin JP, *et al*. Enhancing catalytic activity of perovskite-based catalysts in three-way catalysis by surface composition optimisation. *Catal Today* 2015, **258**: 543–548.

[32] Polo-Garzon F, Wu ZL. Acid-base catalysis over perovskites: A review. *J Mater Chem A* 2018, **6**: 2877–2894.

[33] Wu TJ, Gao P. Development of perovskite-type materials for thermoelectric application. *Materials* 2018, **11**: 999.

[34] Lee KH, Kim SW, Ohta H, *et al*. Thermoelectric properties of layered perovskite-type $(Sr_{1-x}Ca_x)_3(Ti_{1-y}Nb_y)_2O_7$. *J Appl Phys* 2007, **101**: 083707.

[35] Lee KH, Ohta H, Koumoto K, Thermoelectric properties of layered perovskite-type Nb-doped $SrO(SrTiO_3)_n$ (n = 1, 2) ruddlesden-popper phases, In: Proceedings of the 2006 25th International Conference on Thermoelectrics, 2006: 81–84.

[36] Li Q, Zhao H, Huo LH, *et al*. Electrode properties of Sr doped La_2CuO_4 as new cathode material for intermediate-temperature SOFCs. *Electrochem Commun* 2007, **9**: 1508–1512.

[37] Ghorbani-Moghadam T, Kompany A, Bagheri-Mohagheghi MM, *et al*. High temperature electrical conductivity and electrochemical investigation of $La_{2-x}Sr_xCoO_4$ nanoparticles for IT-SOFC cathode. *Ceram Int* 2018, **44**: 21238–21248.

[38] Garali M, Kahlaoui M, Mohammed B, *et al*. Synthesis, characterization and electrochemical properties of $La_{2-x}Eu_xNiO_{4+\delta}$ ruddlesden-popper-type layered nickelates as cathode materials for SOFC applications. *Int J Hydrogen Energ* 2019, **44**: 11020–11032.

[39] Sandoval MV, Pirovano C, Capoen E, *et al*. In-depth study of the Ruddlesden–Popper $La_xSr_{2-x}MnO_{4\pm\delta}$ family as possible electrode materials for symmetrical SOFC. *Int*

J Hydrogen Energ 2017, **42**: 21930–21943.
[40] Monika DL, Nagabhushana H, Krishna RH, *et al*. Synthesis and photoluminescence properties of a novel Sr_2CeO_4:Dy^{3+} nanophosphor with enhanced brightness by Li^+ co-doping. *RSC Adv* 2014, **4**: 38655–38662.
[41] Srinivas M, Appa Rao B, Vithal M, *et al*. Luminescence properties of Tb^{3+} doped Sr_2SnO_4 green phosphor in UV/VUV regions. *Luminescence* 2013, **28**: 597–601.
[42] Xu XH, Wang YH, Gong Y, *et al*. Effect of oxygen vacancies on the red phosphorescence of Sr_2SnO_4:Sm^{3+} phosphor. *Opt Express* 2010, **18**: 16989.
[43] Meeporn K, Chanlek N, Thongbai P. Effects of DC bias on non-ohmic sample-electrode contact and grain boundary responses in giant-permittivity $La_{1.7}Sr_{0.3}Ni_{1-x}Mg_xO_4$ ceramics. *RSC Adv* 2016, **6**: 91377–91385.
[44] Jia BW, Yang WZ, Liu XQ, *et al*. Giant dielectric response in $(Sm_{1-x}Nd_x)_{1.5}Sr_{0.5}NiO_4$ ceramics: The intrinsic and extrinsic effects. *J Appl Phys* 2012, **112**: 024104.
[45] Liu XQ, Wu YJ, Chen XM, *et al*. Temperature-stable giant dielectric response in orthorhombic samarium strontium nickelate ceramics. *J Appl Phys* 2009, **105**: 054104.
[46] Chen YN, Sun Y, Peng JJ, *et al*. 2D ruddlesden-popper perovskites for optoelectronics. *Adv Mater* 2018, **30**: 1703487.
[47] Spanopoulos I, Hadar I, Ke WJ, *et al*. Uniaxial expansion of the 2D Ruddlesden–Popper perovskite family for improved environmental stability. *J Am Chem Soc* 2019, **141**: 5518–5534.
[48] Ganguly P, Rao CNR. Crystal chemistry and magnetic properties of layered metal oxides possessing the K_2NiF_4 or related structures. *J Solid State Chem* 1984, **53**: 193–216.
[49] Rao CNR, Ganguly P, Singh KK, *et al*. A comparative study of the magnetic and electrical properties of perovskite oxides and the corresponding two-dimensional oxides of K_2NiF_4 structure. *J Solid State Chem* 1988, **72**: 14–23.
[50] Rao CNR. *Trends in Chemistry of Materials*. World Scientific, 2008.
[51] Bednorz JG, Müller KA. Possible high T_c superconductivity in the Ba–La–Cu–0 system. *Z. Physik B - Condensed Matter* 1986, **64**: 189–193.
[52] Chroneos A, Vovk RV, Goulatis IL, *et al*. Oxygen transport in perovskite and related oxides: A brief review. *J Alloys Compd* 2010, **494**: 190–195.
[53] Lee D, Lee H. Controlling oxygen mobility in Ruddlesden–Popper oxides. *Materials* 2017, **10**: 368.
[54] Chen BH. Introduction of a tolerance factor for the Nd_2CuO_4(T')-type structure. *J Solid State Chem* 1996, **125**: 63–66.
[55] Mazo GN, Mamaev YA, Galin MZ, *et al*. Structural and transport properties of the layered cuprate Pr_2CuO_4. *Inorg Mater* 2011, **47**: 1218–1226.
[56] Wilhelm H, Cros C, Reny E, *et al*. Pressure-induced structural phase transitions in $Ln_{2-x}Nd_xCuO_4$ for Ln=La ($0.6 \le x \le 2$) and Ln=Pr (x=0). *J Solid State Chem* 2000, **151**: 231–240.
[57] Goldschmidt VM. Die gesetze der krystallochemie. *Naturwissenschaften* 1926, **14**: 477–485.
[58] Rodriguez-Carvajal J, Fernandez-Diaz MT, Martinez JL. Neutron diffraction study on structural and magnetic properties of La_2NiO_4. *J Phys: Condens Matter* 1991, **3**: 3215–3234.
[59] Shannon RD. Revised effective ionic radii and systematic studies of interatomic distances in halides and chalcogenides. *Acta Cryst* 1976, **A32**: 751–767.
[60] Allanyon C, Rodríguez-Carvajal J, Fernández-Díaz MT, *et al*. Crystal structure of the high temperature phase of oxidised $Pr_2NiO_{4+\delta}$. *Z Phys B - Condensed Matter* 1996, **100**: 85–90.
[61] Rice DE, Buttrey DJ. An X-ray diffraction study of the oxygen content phase diagram of $La_2NiO_{4+\delta}$. *J Solid State Chem* 1993, **105**: 197–210.
[62] Allancon C, Gonthiervassal A, Bascat J, *et al*. Influence of oxygen on structural transitions in $Pr_2NiO_{4+\delta}$. *Solid State Ionics* 1994, **74**: 239–248.
[63] Flura A, Dru S, Nicollet C, *et al*. Chemical and structural changes in $Ln_2NiO_{4+\delta}$ (Ln=La, Pr or Nd) lanthanide nickelates as a function of oxygen partial pressure at high temperature. *J Solid State Chem* 2015, **228**: 189–198.
[64] Kröger FA, Vink HJ. Relations between the concentrations of imperfections in crystalline solids. *Solid State Phys* 1956, **3**: 307–435.
[65] Zhao H, Li Q, Sun LP. Ln_2MO_4 cathode materials for solid oxide fuel cells. *Sci China Chem* 2011, **54**: 898–910.
[66] Choisnet J, Mouron P, Crespin M, *et al*. Perovskite-like intergrowth structure of the reduced cuprate $Nd_2CuO_{3.5}$: A combination of defect and excess oxygen non-stoichiometry phenomena. *J Mater Chem* 1994, **4**: 895–898.
[67] Parfitt D, Chroneos A, Kilner JA, *et al*. Molecular dynamics study of oxygen diffusion in $Pr_2NiO_{4+\delta}$. *Phys Chem Chem Phys* 2010, **12**: 6834–6836.
[68] Kieda N. Nonstoichiometry and electrical properties of La_2CuO_4 and $La_2(Cu,Ni)O_4$. *Solid State Ionics* 1991, **49**: 85–88.
[69] Lobo RC, Berry FJ, Greaves C. The synthesis and structural characterization of Sr_2CuO_{4-x}, x □ 0.1. *J Solid State Chem* 1990, **88**: 513–519.
[70] Tamura H, Hayashi A, Ueda Y. Phase diagram of $La_2NiO_{4+\delta}$ ($0 \le \delta \le 0.18$). *Phys C: Supercond* 1993, **216**: 83–88.
[71] Hernden BC, Lussier JA, Bieringer M. Topotactic solid-state metal hydride reductions of Sr_2MnO_4. *Inorg Chem* 2015, **54**: 4249–4256.
[72] Broux T, Bahout M, Hernandez O, *et al*. Reduction of Sr_2MnO_4 investigated by high temperature *in situ* neutron powder diffraction under hydrogen flow. *Inorg Chem* 2013, **52**: 1009–1017.
[73] Sun LP, Li Q, Zhao H, *et al*. Preparation and electrochemical properties of Sr-doped Nd_2NiO_4 cathode materials for intermediate-temperature solid oxide fuel cells. *J Power Sources* 2008, **183**: 43–48.
[74] Kanai H, Mizusaki J, Tagawa H, *et al*. Defect chemistry

of $La_{2-x}Sr_xCuO_{4-\delta}$: Oxygen nonstoichiometry and thermodynamic stability. *J Solid State Chem* 1997, **131**: 150–159.

[75] Khandale AP, Bhoga SS, Kumar RV. Effect of Ni doping on structural, electrical and electrochemical properties of $Nd_{1.8}Ce_{0.2}Cu_{1-x}Ni_xO_{4+\delta}$ mixed ionic–electronic conductor. *Solid State Ionics* 2013, **238**: 1–6.

[76] Khandale AP, Bansod MG, Bhoga SS. Improved electrical and electrochemical performance of co-doped $Nd_{1.8}Sr_{0.2}Ni_{1-x}Cu_xO_{4+\delta}$. *Solid State Ionics* 2015, **276**: 127–135.

[77] Khandale AP, Bhoga SS. Electrochemical performance of $Nd_{1.8}Ce_{0.2}CuO_{4\pm\delta}$ mixed-ionic–electronic conductor for intermediate solid oxide fuel cells. *Solid State Ionics* 2011, **182**: 82–90.

[78] Rao CNR, Buttrey DJ, Otsuka N, *et al*. Crystal structure and semiconductor-metal transition of the quasi-two-dimensional transition metal oxide, La_2NiO_4. *J Solid State Chem* 1984, **51**: 266–269.

[79] Skinner SJ, Kilner JA. Oxygen diffusion and surface exchange in $La_{2-x}Sr_xNiO_{4+\delta}$. *Solid State Ionics* 2000, **135**: 709–712.

[80] Nikonov AV, Kuterbekov KA, Bekmyrza K, *et al*. A brief review of conductivity and thermal expansion of perovskite-related oxides for SOFC cathode. *Eurasian J Phys Funct Mater* 2018, **2**: 274–292.

[81] Wilk P. Structural and electrical properties of $LiNi_{1-y}Co_yO_2$. *Solid State Ionics* 2003, **157**: 109–114.

[82] Cleave AR, Kilner JA, Skinner SJ, *et al*. Atomistic computer simulation of oxygen ion conduction mechanisms in La_2NiO_4. *Solid State Ionics* 2008, **179**: 823–826.

[83] Norimatsu W, Koyama Y. Evolution of orthorhombic domain structures during the tetragonal-to-orthorhombic phase transition in the layered perovskite $Sr_{2-x}La_xMnO_4$. *Phys Rev B* 2006, **74**: 085113.

[84] McCabe EE, Greaves C. Synthesis and structural and magnetic characterization of mixed manganese–copper $n = 1$ ruddlesden–popper phases. *Chem Mater* 2006, **18**: 5774–5781.

[85] Negri B, Leoni M, Hassen RB. Synthesis, structural and electrical characterizations of $LaSrCu_{0.4}Al_{0.6}O_{4-\delta}$. *Mater Renew Sustain Energy* 2017, **6**: 22.

[86] Paolone A, Giura P, Calvani P, *et al*. Charge-localization effects in the infrared transmittance of layered perovskites. *Phys B: Condens Matter* 1998, **244**: 33–40.

[87] Midouni A, Houchati MI, Othman WB, *et al*. Influence of nickel doping on oxygen-ionic conductivity of the $n = 1$ Ruddlesden–Popper phases $La_{1.85}Ca_{0.15}(Cu_{1-x}Ni_x)O_{4-\delta}$ (δ=0.0905). *J Solid State Chem* 2016, **240**: 101–108.

[88] Opila EJ, Tuller HL, Wuensch BJ, *et al*. Oxygen tracer diffusion in $La_{2-x}Sr_xCuO_{4-y}$ single crystals. *J Am Ceram Soc* 1993, **76**: 2363–2369.

[89] Bochkov DM, Kharton VV, Kovalevsky AV, *et al*. Oxygen permeability of $La_2Cu(Co)O_{4+\delta}$ solid solutions. *Solid State Ionics* 1999, **120**: 281–288.

[90] Kharton VV, Viskup AP, Naumovich EN, *et al*. Oxygen ion transport in La_2NiO_4-based ceramics. *J Mater Chem* 1999, **9**: 2623–2629.

[91] Chroneos A, Yildiz B, Tarancón A, *et al*. Oxygen diffusion in solid oxide fuel cell cathode and electrolyte materials: Mechanistic insights from atomistic simulations. *Energy Environ Sci* 2011, **4**: 2774–2789.

[92] Mazo GN, Savvin SN. The molecular dynamics study of oxygen mobility in $La_{2-x}Sr_xCuO_{4-\delta}$. *Solid State Ionics* 2004, **175**: 371–374.

[93] Savvin SN, Mazo GN, Ivanov-Schitz AK. Simulation of ion transport in layered cuprates $La_{2-x}Sr_xCuO_{4-\delta}$. *Crystallogr Rep* 2008, **53**: 291–301.

[94] Chroneos A, Parfitt D, Kilner JA, *et al*. Anisotropic oxygen diffusion in tetragonal $La_2NiO_{4+\delta}$: Molecular dynamics calculations. *J Mater Chem* 2010, **20**: 266–270.

[95] Sayers R, de Souza RA, Kilner JA, *et al*. Low temperature diffusion and oxygen stoichiometry in lanthanum nickelate. *Solid State Ionics* 2010, **181**: 386–391.

[96] Shirani-Faradonbeh H, Paydar MH. Electrical behavior of the Ruddlesden–Popper phase, $(Nd_{0.9}La_{0.1})_2Ni_{0.75}Cu_{0.25}O_4$ (NLNC) and NLNC–x wt% $Sm_{0.2}Ce_{0.8}O_{1.9}$ (SDC) (x=10, 30 and 50), as intermediate-temperature solid oxide fuel cells cathode. *Ceram Int* 2018, **44**: 1971–1977.

[97] Li SL, Tu HY, Li F, *et al*. Investigation of $Nd_2Ni_{0.9}M_{0.1}O_{4+\delta}$ (M=Ni, Co, Cu, Fe, and Mn) cathodes for intermediate-temperature solid oxide fuel cell. *J Alloys Compd* 2017, **694**: 17–23.

[98] Wang YP, Xu Q, Huang DP, *et al*. Diagnosis on improved electrocatalytic activity of $La_2Ni_{0.8}Cu_{0.2}O_{4+\delta}$ electrodes towards oxygen reduction reaction. *Appl Surf Sci* 2017, **423**: 995–1002.

[99] Zheng K, Świerczek K. Evaluation of $La_2Ni_{0.5}Cu_{0.5}O_{4+\delta}$ and $Pr_2Ni_{0.5}Cu_{0.5}O_{4+\delta}$ ruddlesden-popper-type layered oxides as cathode materials for solid oxide fuel cells. *Mater Res Bull* 2016, **84**: 259–266.

[100] Wang YP, Xu Q, Huang DP, *et al*. Survey on electrochemical properties of $La_{2-x}Sr_xNiO_{4\pm\delta}$ (x=0.2 and 0.8, δ>0) cathodes related with structural stability under cathodic polarization conditions. *Int J Hydrogen Energ* 2017, **42**: 6290–6302.

[101] Zhang X, Zhang LF, Meng JL, *et al*. Highly enhanced electrochemical property by Mg-doping $La_2Ni_{1-x}Mg_xO_{4+\delta}$ (x=0.0, 0.02, 0.05 and 0.10) cathodes for intermediate-temperature solid oxide fuel cells. *Int J Hydrogen Energ* 2017, **42**: 29498–29510.

[102] Bhoga SS, Khandale AP, Pahune BS. Investigation on $Pr_{2-x}Sr_xNiO_{4+\delta}$ (x=0.3–1.0) cathode materials for intermediate temperature solid oxide fuel cell. *Solid State Ionics* 2014, **262**: 340–344.

[103] Bansod MB, Khandale AP, Kumar RV, *et al*. Crystal structure, electrical and electrochemical properties of Cu co-doped $Pr_{1.3}Sr_{0.7}NiO_{4+\delta}$ mixed ionic-electronic conductors (MIECs). *Int J Hydrogen Energ* 2018, **43**: 373–384.

[104] Chaudhari VN, Khandale AP, Bhoga SS. An investigation on strontium doped $Sm_2NiO_{4+\delta}$ cathode for intermediate temperature solid oxide fuel cells. *J Power Sources* 2014, **248**: 647–654.

[105] Cao Y, Gu HT, Chen H, *et al*. Preparation and characterization of $Nd_{2-x}Sr_xCoO_{4+\delta}$ cathodes for intermediate-temperature solid oxide fuel cell. *Int J Hydrogen Energ* 2010, **35**: 5594–5600.

[106] Zharikova EV, Rozova MG, Kazakov SM, *et al*. Crystal structure and high-temperature properties of $(Pr,Sr)_2(Co,Mn)O_{4\pm\delta}$ with K_2NiF_4-type structure. *Solid State Commun* 2016, **245**: 31–35.

[107] Zheng K, Gorzkowska-Sobaś A, Świerczek K. Evaluation of Ln_2CuO_4 (Ln: La, Pr, Nd) oxides as cathode materials for IT-SOFCs. *Mater Res Bull* 2012, **47**: 4089–4095.

[108] Mazo GN, Kazakov SM, Kolchina LM, *et al*. Thermal expansion behavior and high-temperature electrical conductivity of $A_{2-x}A'_xCu_{1-y}Co_yO_{4\pm\delta}$ (A=La, Pr; A'=Pr, Sr) oxides with the K_2NiF_4-type structure. *J Alloys Compd* 2015, **639**: 381–386.

[109] Chaudhari VN, Khandale AP, Bhoga SS. Synthesis and characterization of Ce-doped $Sm_2CuO_{4+\delta}$ cathode for IT-SOFC applications. *Ionics* 2017, **23**: 2553–2560.

[110] Zhou J, Chen G, Wu K, *et al*. The performance of $La_{0.6}Sr_{1.4}MnO_4$ layered perovskite electrode material for intermediate temperature symmetrical solid oxide fuel cells. *J Power Sources* 2014, **270**: 418–425.

[111] Sandoval MV, Durán S, Prada A, *et al*. Synthesis and preliminary study of $Nd_xAE_{2-x}MnO_{4\pm\delta}$ (AE: Ca, Sr) for symmetrical SOFC electrodes. *Solid State Ionics* 2018, **317**: 194–200.

[112] Fujii K, Shiraiwa M, Esaki Y, *et al*. Improved oxide-ion conductivity of $NdBaInO_4$ by Sr doping. *J Mater Chem A* 2015, **3**: 11985–11990.

[113] Yang XY, Liu SB, Lu FQ, *et al*. Acceptor doping and oxygen vacancy migration in layered perovskite $NdBaInO_4$-based mixed conductors. *J Phys Chem C* 2016, **120**: 6416–6426.

[114] Lunkenheimer P, Fichtl R, Ebbinghaus SG, *et al*. Nonintrinsic origin of the colossal dielectric constants in $CaCu_3Ti_4O_{12}$. *Phys Rev B* 2004, **70**: 172102.

[115] Raevski IP, Prosandeev SA, Bogatin AS, *et al*. High dielectric permittivity in $AFe_{1/2}B_{1/2}O_3$ nonferroelectric perovskite ceramics (A=Ba, Sr, Ca; B=Nb, Ta, Sb). *J Appl Phys* 2003, **93**: 4130–4136.

[116] Bobnar V, Lunkenheimer P, Paraskevopoulos M, *et al*. Separation of grain boundary effects and intrinsic properties in perovskite-like $Gd_{0.6}Y_{0.4}BaCo_2O_{5.5}$ using high-frequency dielectric spectroscopy. *Phys Rev B* 2002, **65**: 184403.

[117] Iguchi E, Mochizuki S. Electric conduction and dielectric relaxation processes in solid oxide fuel cell electrolyte $La_{0.5}Sr_{0.5}Ga_{0.6}Ti_{0.4}O_{3-\delta}$. *J Appl Phys* 2004, **96**: 3889–3895.

[118] Lunkenheimer P, Krohns S, Riegg S, *et al*. Colossal dielectric constants in transition-metal oxides. *Eur Phys J Spec Top* 2009, **180**: 61–89.

[119] Lunkenheimer P, Bobnar V, Pronin AV, *et al*. Origin of apparent colossal dielectric constants. *Phys Rev B* 2002, **66**: 052105.

[120] Sinclair DC, Adams TB, Morrison FD, *et al*. $CaCu_3Ti_4O_{12}$: One-step internal barrier layer capacitor. *Appl Phys Lett* 2002, **80**: 2153–2155.

[121] Cohen MH, Neaton JB, He LX, *et al*. Extrinsic models for the dielectric response of $CaCu_3Ti_4O_{12}$. *J Appl Phys* 2003, **94**: 3299–3306.

[122] Tlili MT, Chihaoui N, Bejar M, *et al*. Charge ordering analysis by electrical and dielectric measurements in $Ca_{2-x}Pr_xMnO_4$ (x=0–0.2) compounds. *J Alloys Compd* 2011, **509**: 6447–6451.

[123] Sternlieb BJ, Hill JP, Wildgruber UC, *et al*. Charge and magnetic order in $La_{0.5}Sr_{1.5}MnO_4$. *Phys Rev Lett* 1996, **76**: 2169–2172.

[124] Chouket A, Cheikhrouhou-Koubaa W, Cheikhrouhou A, *et al*. Structural, microstructural and dielectric studies in multiferroic $LaSrNiO_{4-\delta}$ prepared by mechanical milling method. *J Alloys Compd* 2016, **662**: 467–474.

[125] Chouket A, Optasanu V, Bidault O, *et al*. Dielectric relaxation and polaronic hopping in Mn-substituted $LaSrNiO_4$ nickelates prepared by mechanical milling method. *J Alloys Compd* 2016, **688**: 163–172.

[126] Wang J, Liu G, Jia BW, *et al*. Giant dielectric response and polaronic hopping in Al-substituted $A_{5/3}Sr_{1/3}NiO_4$ (A=La, Nd) ceramics. *Ceram Int* 2014, **40**: 5583–5590.

[127] Song CL, Wu YJ, Liu XQ, *et al*. Dielectric properties of $La_{1.75}Ba_{0.25}NiO_4$ ceramics prepared by spark plasma sintering. *J Alloys Compd* 2010, **490**: 605–608.

[128] Shi CY, Hu ZB, Hao YM. Structural, magnetic and dielectric properties of $La_{2-x}Ca_xNiO_{4+\delta}$ (x = 0, 0.1, 0.2, 0.3). *J Alloys Compd* 2011, **509**: 1333–1337.

[129] Krohns S, Lunkenheimer P, Kant C, *et al*. Colossal dielectric constant up to gigahertz at room temperature. *Appl Phys Lett* 2009, **94**: 122903.

[130] Liu G, Liu XQ, Chen XM. Contribution of oxygen vacancies to the giant dielectric response in $Sm_{1.5}Sr_{0.5}NiO_{4-\delta}$ ceramics. *Appl Phys A* 2014, **116**: 1421–1427.

[131] Thongbai P, Yamwong T, Maensiri S. Microstructure and modified giant dielectric response in Ga-doped $La_{1.5}Sr_{0.5}NiO_4$ ceramics. *Mater Lett* 2012, **82**: 244–247.

[132] Chupakhina TI, Melnikova NV, Gyrdasova OI. Synthesis, structural characteristics and dielectric properties of a new K_2NiF_4-type phase $Sr_2Mn_{0.5}Ti_{0.5}O_4$. *J Alloys Compd* 2016, **670**: 105–112.

[133] Mira J, Castro-Couceiro A, Sánchez-Andújar M, *et al*. High dielectric constant in charge-ordered $Ca_{1.75}Pr_{0.25}MnO_4$. *J Phys D: Appl Phys* 2006, **39**: 1192–1196.

[134] Ren GR, Zhu JY, Li L, *et al*. $SrLa(R_{0.5}Ti_{0.5})O_4$ (R = Mg, Zn) microwave dielectric ceramics with complex K_2NiF4 -type layered perovskite structure. *J Am Ceram Soc* 2017, **100**: 2582–2589.

[135] Xiao Y, Chen XM, Liu XQ. Stability and microwave dielectric characteristics of $(Ca_{1-x}Sr_x)LaAlO_4$ ceramics. *J Electroceram* 2008, **21**: 154–159.

[136] Liu B, Yi L, Liu XQ, *et al*. Structure and microwave dielectric properties of $SrSmAlO_4$–Sr_2TiO_4 solid solutions. *J Electroceram* 2015, **34**: 114–121.

[137] Mao MM, Fan XC, Chen XM. Effect of A-site ionic radius on the structure and microwave dielectric

characteristics of $Sr_{1+x}Sm_{1-x}Al_{1-x}Ti_xO_4$ ceramics. *Int J Appl Ceram Technol* 2010, **7**: E156–E162.

[138] Zhang C, Yi L, Li L, *et al*. Structure and microwave dielectric characteristics of solid solutions in $SrNdAlO_4$–Sr_2TiO_4 system. *Int J Appl Ceram Technol* 2013, **10**: E70–E76.

[139] Yuan HX, Chen XM, Mao MM. Structure and microwave dielectric characteristics of $Ca_{1+x}Nd_{1-x}Al_{1-x}Ti_xO_4$ ceramics. *J Am Ceram Soc* 2009, **92**: 2286–2290.

[140] Mao MM, Liu XQ, Chen XM. Structural evolution and its effects on dielectric loss in $Sr_{1+x}Sm_{1-x}Al_{1-x}Ti_xO_4$ microwave dielectric ceramics. *J Am Ceram Soc* 2011, **94**: 2506–2511.

[141] Luo Y, Zhang J, Yue ZX, *et al*. Improvement in microwave dielectric properties of Sr_2TiO_4 ceramics through post-annealing treatment. *J Electroceram* 2018, **41**: 67–72.

[142] Liu B, Li L, Liu XQ, *et al*. $Sr_{n+1}Ti_nO_{3n+1}$ (n=1, 2) microwave dielectric ceramics with medium dielectric constant and ultra-low dielectric loss. *J Am Ceram Soc* 2017, **100**: 496–500.

[143] Balachandran PV, Puggioni D, Rondinelli JM. Crystal-chemistry guidelines for noncentrosymmetric A_2BO_4 ruddlesden–popper oxides. *Inorg Chem* 2014, **53**: 336–348.

[144] Benedek NA, Mulder AT, Fennie CJ. Polar octahedral rotations: A path to new multifunctional materials. *J Solid State Chem* 2012, **195**: 11–20.

[145] Mulder AT, Benedek NA, Rondinelli JM, *et al*. Turning ABO_3 antiferroelectrics into ferroelectrics: Design rules for practical rotation-driven ferroelectricity in double perovskites and $A_3B_2O_7$ ruddlesden-popper compounds. *Adv Funct Mater* 2013, **23**: 4810–4820.

[146] Xiao Y, Chen XM, Liu XQ. Microstructures and microwave dielectric characteristics of $CaRAlO_4$ (R=Nd, Sm, Y) ceramics with tetragonal K_2NiF_4 structure. *J Am Ceram Soc* 2005, **87**: 2143–2146.

[147] Liu XQ, Chen XM. Microwave dielectric characteristics of $SrLaGaO_4$ and $SrNdGaO_4$ ceramics. *J Eur Ceram Soc* 2006, **26**: 1969–1971.

[148] Monika DL, Nagabhushana H, Nagabhushana BM, *et al*. One pot auto-ignition based synthesis of novel Sr_2CeO_4:Ho^{3+} nanophosphor for photoluminescent applications. *J Alloys Compd* 2015, **648**: 1051–1059.

[149] Srinivas M, Tamboli S, Dhoble SJ. VUV-UV photoluminescence properties of Ce^{3+} doped Ca_2SnO_4 phosphor for PDP application. *Optik* 2017, **145**: 202–208.

[150] Yamashita T, Ueda K. Blue photoluminescence in Ti-doped alkaline-earth stannates. *J Solid State Chem* 2007, **180**: 1410–1413.

[151] Shi MM, Zhang DY, Chang CK. Dy^{3+}:Ca_2SnO_4, a new yellow phosphor with afterglow behavior. *J Alloys Compd* 2015, **639**: 168–172.

[152] Lei BF, Zhang HR, Mai WJ, *et al*. Luminescent properties of orange-emitting long-lasting phosphorescence phosphor Ca_2SnO_4:Sm^{3+}. *Solid State Sci* 2011, **13**: 525–528.

[153] Lei BF, Yue S, Zhang YZ, *et al*. Luminescence properties of Sr_2SnO_4:Sm^{3+} afterglow phosphor. *Chinese Phys Lett* 2010, **27**: 037201.

[154] Yang HM, Shi JX, Gong ML. A new luminescent material, Sr_2SnO_4:Eu^{3+}. *J Alloys Compd* 2006, **415**: 213–215.

[155] Kamimura S, Yamada H, Xu CN. Purple photochromism in Sr_2SnO_4:Eu^{3+} with layered perovskite-related structure. *Appl Phys Lett* 2013, **102**: 031110.

[156] Khadraoui Z, Horchani-Naifer K, Ferhi M, *et al*. Electronic structure and optical properties of $TbPO_4$: Experiment and density functional theory calculations. *Opt Mater* 2015, **47**: 484–489.

[157] Li HF, Jia YL, Sun WZ, *et al*. Novel energy transfer mechanism in single-phased color-tunable Sr_2CeO_4:Eu^{3+} phosphors for WLEDs. *Opt Mater* 2014, **36**: 1883–1889.

[158] Seo YW, Noh HM, Moon BK, *et al*. Structural and luminescent properties of blue-emitting Sr_2CeO_4 phosphors by high-energy ball milling method. *Ceram Int* 2015, **41**: 1249–1254.

[159] Xiao QL, Chen WY. Ultraviolet to near-infrared conversion in Nd^{3+} doped strontium cerate nanophosphors. *J Alloys Compd* 2015, **631**: 272–275.

[160] Guan L, Jia GQ, Yang BZ, *et al*. Synthesis and optical properties of Dy^{3+}, Li^+ doped $CaMoO_4$ phosphor. *J Rare Earth* 2011, **29**: 540–543.

[161] Du QQ, Zhou GJ, Zhou J, *et al*. Enhanced luminescence of novel $Y_2Zr_2O_7$:Dy^{3+} phosphors by Li^+ co-doping. *J Alloys Compd* 2013, **552**: 152–156.

[162] Balakrishnaiah R, Yi SS, Jang K, *et al*. Enhanced luminescence properties of YBO_3:Eu^{3+} phosphors by Li-doping. *Mater Res Bull* 2011, **46**: 621–626.

[163] Zhang LX, Jiu HF, Fu YH, *et al*. Preparation and photoluminescence enhancement of Li^+ and Eu^{3+} co-doped YPO_4 hollow microspheres. *J Rare Earth* 2013, **31**: 449–455.

Open Access This article is licensed under a Creative Commons Attribution 4.0 International License, which permits use, sharing, adaptation, distribution and reproduction in any medium or format, as long as you give appropriate credit to the original author(s) and the source, provide a link to the Creative Commons licence, and indicate if changes were made.

The images or other third party material in this article are included in the article's Creative Commons licence, unless indicated otherwise in a credit line to the material. If material is not included in the article's Creative Commons licence and your intended use is not permitted by statutory regulation or exceeds the permitted use, you will need to obtain permission directly from the copyright holder.

To view a copy of this licence, visit http://creativecommons.org/licenses/by/4.0/.